nature sustainability

Article

https://doi.org/10.1038/s41893-025-01657-y

Photoluminescent radiative cooling for aesthetic and urban comfort

Received: 19 March 2025

Accepted: 10 September 2025

Published online: 07 October 2025

Check for updates

Yang Fu[1], Xue Ma[2], Xiao-Wen Zhang[3], Ze Li[1], Chuyao Wang[1], Kaixin Lin[1], Yiying Zhou[1], Aiqiang Pan[1], Xu Chen[1], Xin Li[1], Wenqi Wang[1], Chui Ting Kwok[1], Yi-Hao Zhu[1], Xiao Xue[4], Xin Zhao[2], Andrey L. Rogach[2,5], Longnan Li[3], Wei Li[3] ✉ & Chi Yan Tso[1] ✉

Passive radiative cooling offers a sustainable solution to reduce carbon emissions in space cooling by simultaneously reflecting sunlight and emitting thermal radiation. However, the super-white property of conventional passive radiative cooling materials poses challenges for large-scale urban applications by conflicting with aesthetic requirements and neglecting impacts on urban microclimate and pedestrian thermal and visual comfort. Here inspired by the biological photoadaptation of coral, we present photoluminescence-based aesthetic composites as innovative urban skins that harness the enhanced light conversion of rare-earth-doped phosphors while decoupling from light-scattering-based whiteness, providing cool colours with improved urban compatibility. These composites demonstrate effective spectral reflectance of over 100% and peak reflectance up to 141% in their emission regions, despite a moderate overall solar reflectance (90.2–93.2%). With vivid yet angle-insensitive green, yellow and red appearances, the composites achieve subambient temperature reductions of 2.2–3.7 °C compared with ambient air and 6.1–7.9 °C relative to their non-photoluminescent counterparts. Moreover, their moderate whiteness alleviates excessive thermal and visual stress induced by trapping of sunlight in urban environments. Featuring excellent durability, compatibility and stability, these composites offer a scalable solution for energy-efficient and aesthetically pleasing radiative cooling in architecture, textiles and beyond, advancing passive radiative cooling technologies towards diverse real-world implementations.

The pressing global challenges of energy scarcity and climate change demand transformative innovations in cooling technologies that minimize energy consumption and carbon emissions[1,2]. Passive radiative cooling (PRC) emerges as a groundbreaking solution, leveraging the thermodynamic link of the Earth to the cryogenic universe (~2.7 K) via infrared (IR) thermal radiation[3–8]. By simultaneously reflecting sunlight and emitting thermal energy in the atmospheric transparency window, PRC achieves a net radiative heat loss, enabling subambient surface temperatures[9–12]. Beyond space cooling, PRC has crucial implications for diverse applications, including personal thermal management, water harvesting and energy generation/storage[13–18]. Since the breakthrough in demonstrating daytime PRC, this disruptive technology has garnered unprecedented global traction, with its market size predicted to surpass US$76.7 billion by the end of 2030 at a compound annual growth rate of 9.48%, outpacing conventional heating, ventilation and air conditioning (HVAC) systems[19,20]. However, wide-scale adoption

A full list of affiliations appears at the end of the paper. ✉e-mail: weili1@ciomp.ac.cn; chiytso@cityu.edu.hk

of PRC materials also raises critical concerns about their potential impact on urban microenvironments, particularly regarding thermal and visual comfort for pedestrians and the broader cityscape, which remain insufficiently evaluated and addressed.

Conventional PRC systems are optimized to reflect the entire solar spectrum to minimize thermal loads and maximize cooling capacities, resulting in a glaring white appearance. Adopting super-white PRC surfaces as urban skins presents aesthetic and visual pollution challenges, potentially causing physical discomfort and psychological strain for individuals[21,22]. On the one hand, the glaring whiteness of PRC materials often fails to meet urban aesthetic demands. On the other hand, the enhanced whiteness of vertical surfaces can intensify sunlight trapping within urban canyons, exacerbating thermal and visual stress for pedestrians by increasing localized heat and glare effects[23,24]. Thus, rendering PRC materials colourful is indispensable for enhancing aesthetic versatility, mitigating urban heat and suppressing glare, particularly for applications in buildings, textiles, vehicles and electronics[25–28]. However, such colouration conflicts with the cooling demands, as only a fraction of the visible (VIS) light responsible for the colour is reflected into human eyes, while the rest is absorbed as heat. Given that VIS light contributes 44% of solar irradiance, while the maximum cooling capacity is ~130 W m^{-2}, even moderate VIS light absorption (~30%) would greatly compromise the potential of PRC materials, restricting the achievable chromaticity[29]. Thus, achieving vibrant, customizable colours in PRC materials while preserving their cooling performance presents a profound and unresolved dilemma[30].

To address this challenge, photoluminescence (PL)-based strategies have emerged as a promising pathway. Unlike structural colouration, which relies on intricate and costly photonic architectures to produce angle-dependent, iridescent appearances[31–33], PL-based approaches offer a more intuitive and cost-effective solution for creating angle-insensitive colours with reduced whiteness and minimal thermal load[34–37]. By harnessing fluorescent phosphors, the absorbed photons can be down-converted into re-emitted photons at longer wavelengths, thereby reducing heat generation, facilitating aesthetic enhancement and simultaneously recovering cooling power. While spectral reflectance can exceed 100% at specific wavelengths, light conversion can suppress the whiteness. Nevertheless, existing PL-based PRC systems are constrained by low chromaticity due to the reliance on highly reflective substrates or matrices, in which subambient cooling is achieved predominantly through the light-scattering-induced whiteness, with only a limited yet unquantified contribution from the light conversion process itself (Supplementary Table 1)[38,39]. Realizing vivid, stable and diverse colours combined with multifunctionality and subambient cooling performance through PL strategies, without relying on super whiteness, remains a critical challenge. Additionally, a critical bottleneck lies in the absence of standardized methodologies to disentangle and precisely quantify the intricate interplay between light conversion and thermal management, as well as the overlooked impact on the urban microenvironment, pedestrian thermal and visual comfort, thereby impeding material optimization and broader adoption.

Here we present a photoluminescence-based aesthetic composite (PLAC) for radiative cooling that fundamentally addresses the long-standing trade-off between the intertwined optical, chromatic, cooling, comfort and functional challenges of coloured PRC for urban skins. By leveraging the light conversion properties of rare-earth-doped phosphors, the PLAC achieves vibrant, customizable and angle-insensitive colours with moderate whiteness while maintaining high cooling efficiency. Through the careful engineering of scattering, both PL enhancement and light conversion efficiency are optimized, effectively resolving the colour-cooling conundrum and overcoming the intrinsic limitations of conventional, light-scattering-based super-white PRC systems. To enable precise optimization, we further introduce a standardized spectro-fluorescence-photometry (SFP) methodology that effectively decouples the light conversion and scattering processes, establishing an analytical tool that has been critically lacking in this field. The optimized PLACs exhibited effective spectral reflectance exceeding 100% and, importantly, a peak reflectance over 140% at the emission wavelength regions. Even with a moderate overall solar reflectance of 90.2–93.2%, the PLACs demonstrated remarkable subambient temperature reductions of 2.2–3.9 °C and net cooling power ranging from 11.9 W m^{-2} to 40.7 W m^{-2} during outdoor field tests. These results unequivocally highlight the immense potential of cooling power recovery through light conversion, effectively circumventing the traditional reliance on the scattering-based whiteness. Through comprehensive assessments using quantitative indicators including mean radiant temperature (MRT), the universal thermal climate index (UTCI) and daylight glare probability (DGP), we demonstrate that the PLACs substantially mitigate the negative thermal and visual impacts of super-white PRC materials on urban microclimates. Specifically, the moderate whiteness of the PLAC reduces MRT by up to 9.3 °C and decreases thermal discomfort periods (TDP) and visual discomfort periods (VDP) by 8.6% and 5.8%, respectively, predominantly through the reduction of excessive shortwave reflection. Along with their exceptional aesthetics, cooling capacities and urban-friendly properties, the PLACs further showcase outstanding compatibility with diverse substrates, excellent mechanical flexibility, long-term durability and robust hydrophobicity. These attributes position PLACs as a transformative solution for practical deployment in the rapidly growing PRC market, paving the way for a more vibrant, energy-efficient and environmentally comfortable residential urban landscape.

Results

Coral polyp-inspired PLAC

Coral reefs, vital ecosystems which support one-quarter of marine species, are primarily built by coral polyps[40]. Reef forming relies on synergistic photosynthetic activity of coral polyps and their algal symbiont under appropriate sunlight. However, low sunlight intensity reduces photosynthetic efficiency, while high intensity brings excessive heat stress, rendering photoinhibition or massive coral bleaching[41]. Coral polyps survived by using photoluminescent pigments in chromatophores to adapt to varying lighting conditions[42–44]. Under low light intensity, polyps expand to let more light penetrate for efficient photosynthetic. Under high light intensity, they contract, with denser pigments and PL emissions, to reduce heat stress[42]. This biological light adaptation inspired the deployment of PL for interconnecting coolness and colouration in PRC materials.

Our PLAC mimics the photobiological construction of coral polyps, comprising a flexible polymer matrix, rare-earth-doped inorganic phosphors and silica nanoparticles (Fig. 1a). The polymer matrix (polydimethylsiloxane (PDMS)) provides high transparency for sunlight and infrared emission enhancement due to its characteristic Si–C (1,246 cm^{-1}), Si–O (1,019 cm^{-1}) and Si–C–H (873 cm^{-1}) bonds[45,46], along with mechanical flexibility and substrate compatibility. Rare-earth-doped inorganic phosphors, including $(Ba, Sr)_2SiO_4$:Eu, $Y_3(Gd, Al)_5O_{12}$:Ce and $(Sr, Ca)AlSiN_3$:Eu for green, yellow and red, respectively (Supplementary Figs. 1 and 2), serve as PL pigments, providing colour generation and light conversion[36,39]. Commercial non-PL pigments (such as iron oxide pigments) generate colour merely through VIS light absorption. Even with enhanced near-infrared (NIR) reflection, the colouration-induced VIS light absorption still contributes to considerable solar heating[47]. On the contrary, PL pigments achieve colouration through a combination of reflected light and fluorescence, effectively reducing solar heating. Hence, PLAC can achieve more vibrant colours and higher overall solar reflectance at the same solar thermal load, as compared with non-PL pigments-based aesthetic composites (NPAC) (Fig. 1b). As shown in Fig. 1c, the emission peaks for three PL pigments are located at 517 nm, 570 nm and 624 nm, respectively,

https://doi.org/10.1038/s41893-025-01657-y

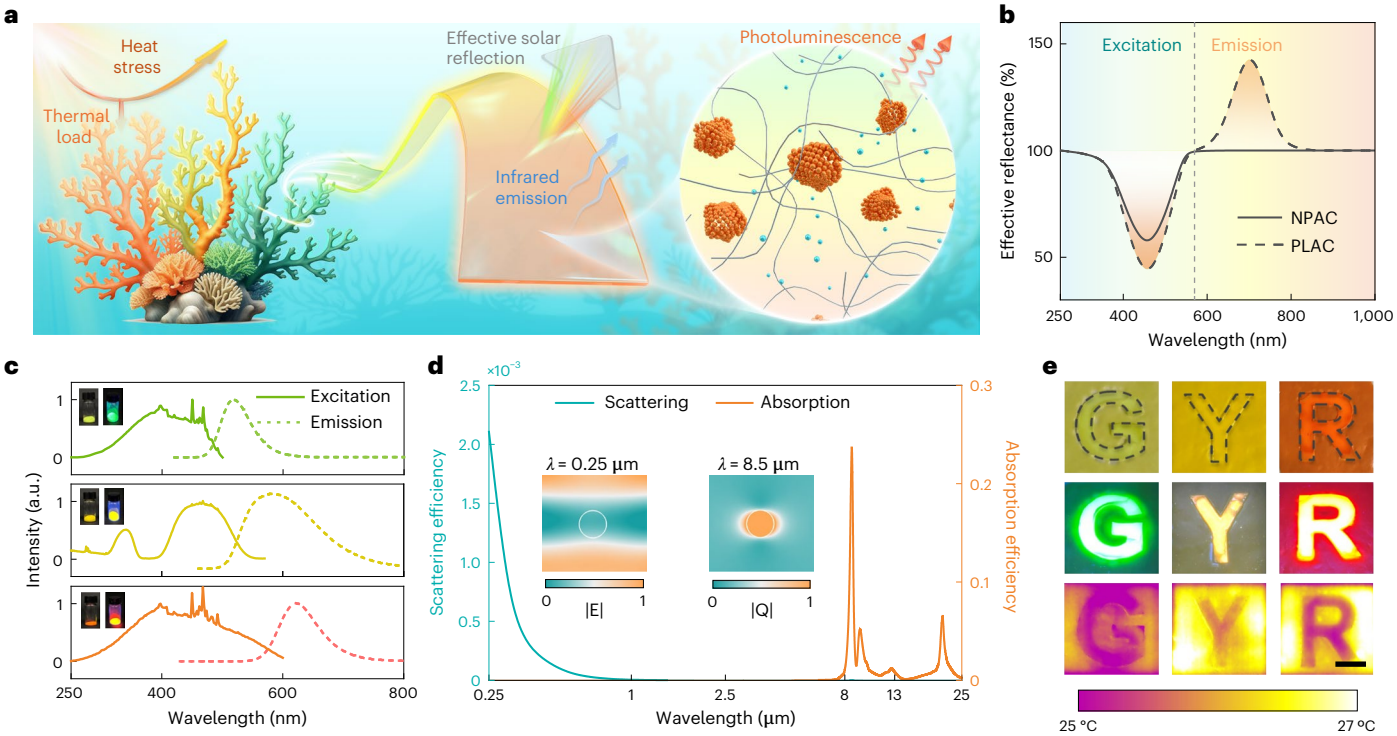

Fig. 1 | Design principle and visual appearance of the PLACs. a, Schematic of coral polyp-inspired PLAC with a polymer matrix, PL pigments and a UV scatterer. The PLAC dissipates heat via mid-IR radiation and reduces thermal load through sunlight scattering and light re-emission. **b**, Schematic comparison between the effective reflectance spectra of NPAC (solid line) and PLAC (dashed line). The NPAC generates colour only through VIS light absorption, which also induces thermal load, while the PLAC absorbs and re-emits light for colouration. **c**, Excitation and emission spectra of green, yellow and red PL pigments. These spectral ranges cover the main part of VIS light. Insets show the optical images of the PL pigments under room light (left) and UV light (right). Bright fluorescence can be observed under UV light. **d**, The scattering and absorption efficiencies of SiO_2 nanoparticles with a diameter of 50 nm. These nanoparticles offer high scattering efficiency at shorter wavelengths, especially in the UV range, and high absorption efficiency in the IR region, contributing to either fluorescence enhancement or IR emissivity improvement. Insets are the normalized electric field |E| at 0.25 μm (left) and electromagnetic loss density |Q| at 8.5 μm. **e**, Comparisons between PLACs and NPACs. The green, yellow and red PLACs are fabricated in the shape of G, Y and R and surrounded by NPACs with similar colours. Under room light (top), PLACs look like NPACs and thereby are visually camouflaged. Under UV light (middle), PLACs present bright fluorescence. Under a sun simulator of ~450 W m^{-2} irradiation (bottom), PLACs reveal clear shapes in the thermal images due to PL-induced cooling enhancement. Scale bar, 3 cm.

thus providing vibrant green, yellow and red luminous colours under ultraviolet (UV) light, while similar apparent colours can be observed under room light. Silica nanoparticles were incorporated to help evenly disperse the micro-sized phosphors through viscosity effects and steric hindrance (Extended Data Fig. 1a). Meanwhile, silica nanoparticles, with the size of 50 nm, contribute to scattering of short-wavelength photons as a result of Rayleigh scattering and IR emission improvement stemming from Si–O–Si bond (459 cm^{-1}), Si–OH bond (900–960 cm^{-1}) and matrix-enhanced absorption efficiency at the Reststrahlen band (1,042–1,242 cm^{-1}) (Fig. 1d, Extended Data Fig. 1b–e and Supplementary Note 3)[48–50]. Moreover, by carefully controlling nanoparticle size, Mie scattering in the VIS range is suppressed to prevent re-absorption by phosphor of PL emissions, while Rayleigh scattering elongates the light path of short-wavelength photons, effectively decoupling scattering-based whiteness from PL enhancement (Extended Data Fig. 2 and Supplementary Fig. 3). As a result, more photons are captured by the PL pigments for excitation, especially under higher volume fraction, leading to increased PL contributions and enhanced light conversion efficiencies (Extended Data Fig. 2 and Supplementary Figs. 4and 5). To showcase the superiority of PLACs, we fabricated three PLACs in the shape of letters G, Y and R and compared their visual appearance with surrounding NPACs (Fig. 1e). Although PLACs and NPACs revealed analogous colours under room light, the shapes of PLACs were exposed through the bright fluorescence under UV light. Additionally, PLACs exhibited lower temperature than NPACs under light irradiation of ~450 W m^{-2}, appearing clearly in the thermal images. This indicates superior chromatic and thermal properties for aesthetic PRC using light conversion.

Precisely decoupled PL emission for optical and chromatic optimization

At the thermodynamic equilibrium state, the net cooling power (P_{net}) of PLACs can be obtained as:

$$P_{net} = P_{rad} - (P_{sun} - P_{PL}) - P_{atm} - P_{nrad} \quad (1)$$

where the incoming heat flows consist of the absorbed sunlight P_{sun}, downward longwave radiation from the atmosphere P_{atm} and non-radiative thermal exchange P_{nrad}, while the outgoing heat flows are the emitted IR radiation P_{rad} and total photoluminescence P_{PL}. The net solar thermal load is denoted as ($P_{sun} - P_{PL}$) (Supplementary Notes 1 and 2). Considering the non-ideal quantum yield and Stokes shift, more PL pigments introduce more light conversion but also inevitable thermal loads[34,51]. As a result, there exists an optimal concentration of PL pigments that delicately balances overall solar reflectance and light conversion efficiency. Meanwhile, accurately characterizing both the spectral solar reflectance and the visual appearance of PLACs remains challenging, because of the misinterpretation of PL emissions.

Generally, for common PRC without PL, the optical properties at the solar spectrum and the chromatic properties are determined by the spectral reflectance[29]. However, for PLACs, using the same

characterization method results in a pseudo spectral reflectance because the converted light would be spectrally misinterpreted, specifically, the re-emitted photons are incorrectly regarded as part of the reflected light due to the lack of proper decoupling (Extended Data Fig. 3a and Supplementary Note 4)[52–54]. Therefore, we suggest an SFP method that can appropriately reconstruct the reflected/converted light in the reflectance spectra, in which the PL emissions are decoupled through a short-pass filter and then quantitatively characterized using a fluorescence photometer (Fig. 2a, Extended Data Fig. 3, Supplementary Note 5 and Supplementary Figs. 6–8). With this method, the effective spectral reflectance and the chromatic properties for PLACs under standard solar irradiation can be reliably determined (Supplementary Notes 6 and 7 and Supplementary Figs. 9–15).

To validate this methodology and optimize the concentration of PL pigments, coloured radiative cooling samples were fabricated. PLACs were integrated onto a typical PRC material (Al_2O_3-doped PDMS coating with a solar reflectance of ~94.9% in this work; Supplementary Fig. 16) to reflect the sunlight transmitted through PLACs for subambient cooling. While increasing the volume fraction of PL pigments, the overall solar reflectance decreases, but the PL contribution to the overall solar reflectance rises (Fig. 2b). This is intuitive because more PL pigments bring more light conversion as well as more thermal load, while the PL contribution grows slower at high-volume fractions. Light conversion efficiency, denoting the ratio between the total energy of re-emitted photons and the absorbed photons, is the key to these nonlinear variations. At low-volume fractions of PL pigments, light conversion is less efficient since the dispersion of PL pigments is too sparse to capture the high-energy photons. However, with higher volume fractions, the high-energy photons can be more efficiently captured and converted by the PL pigments, benefiting from the multiple Rayleigh scattering (Fig. 2c and Supplementary Fig. 4). The light conversion efficiencies approach a plateau at the volume fraction of ~4% and reach the maximum of 54.1%, 53.4% and 62.9% at the volume fraction of around 8% for green, yellow and red PLACs, respectively. Over half the thermal loads for colouration are suppressed.

Meanwhile, the chromatic properties of PLACs obtained from the SFP method align better with our natural colour vision than those of conventional spectrophotometry (Fig. 2d and Supplementary Fig. 14). Higher volume fractions of PL pigments lead to larger chromaticity coordinates in the International Commission on Illumination (CIE) 1931 colour space as well as higher lightness and saturation in the CIE LCh colour space (Supplementary Fig. 15). Further increases in volume fraction (>8%) barely improve light conversion efficiency, leading to linear and parallel elevation of PL contribution, colour saturation and thermal loads. Given that, the volume fraction of ~8% is identified for the optimized PLACs. Through the effective spectral reflectance, we can observe obvious reflectance exceeding 100% due to the light conversion processes (Fig. 2e), which indicates that the total spectral intensity, comprising both reflected and emitted light, surpasses the intensity of the incident light source. This phenomenon occurs only at the emission wavelength ranges and strictly adheres to the principle of energy conservation (Supplementary Fig. 17). Notably, the peak reflectance reaches 141% for the red PLAC, with the potential for even higher values by increasing the concentration of PL pigments. The overall solar reflectance is 91.7%, 93.2% and 90.2%, which reveals reduced whiteness and IR emissivity is 95.0%, 92.3% and 94.6% for green, yellow and red PLACs, respectively (Fig. 2f and Extended Data Fig. 4d–f). Additionally, the PLACs exhibit angle-insensitive coloured appearances, further enhancing their practical applicability (Extended Data Fig. 5 and Supplementary Fig. 18).

Cooling performance and energy saving

Thermal performance measurements are a key indicator of cooling capacity of PRC materials. Indoor measurements of three PLACs together with an individual PRC substrate under a sun simulator (~500 W m^{-2}) were conducted. No obvious temperature increase in PLACs is observed compared with the PRC substrate (Fig. 3a), indicating the minimal thermal loads from PL-induced colouration. Further, outdoor field tests in Changchun (China) were conducted in a thermally insulated acrylic box (Fig. 3b). For comparison, three NPACs with similar colours and a white PRC substrate were included. As shown in Fig. 3c, under sunlight irradiation of 660–750 W m^{-2} (10:00 to 14:00), all PLACs maintained subambient temperatures, whereas NPACs exhibited temperatures above ambient levels. Although the PRC substrate had the lowest temperature, the temperature differences between PLACs and PRC substrate were smaller than those between PLACs and NPACs, since over half the thermal load was removed via light conversion. The green, yellow and red PLACs achieved average temperature reductions (10:00 to 14:00) of 3.7 °C, 3.9 °C and 2.2 °C below ambient air and 7.2 °C, 6.1 °C and 7.8 °C below NPACs, respectively. Our 3-day outdoor tests in Changchun and Hong Kong confirmed stable subambient cooling effects (Extended Data Fig. 6).

Net cooling power calculation showed that PLACs were expected to achieve subambient temperature reductions of 2.0–6.9 °C, 2.9–10.2 °C and 1.1–3.8 °C under varying thermal insulations (non-radiative heat transfer coefficient of 0–12 W m^{-2}; Fig. 3d). The experimental temperature reduction in Fig. 3c indicates a moderate thermal insulation with the non-radiative heat transfer coefficient of around 5 W m^{-2} K^{-1}. Theoretical cooling powers of green, yellow and red PLACs are 33.2 W m^{-2}, 48.5 W m^{-2} and 18.8 W m^{-2}, respectively. Experimental measurement using a home-built feedback control system verified the cooling power (averaged between 11:00 to 15:00) of 28.1 W m^{-2}, 44.4 W m^{-2} and 20.1 W m^{-2} (Fig. 3e and Supplementary Fig. 19), respectively[12]. On the basis of this cooling performance, we evaluated the energy-saving potential for mid-rise apartment buildings with PLAC-covered roofs and walls, adopting typical operation and HVAC systems (Extended Data Fig. 7)[55]. The results indicated cooling energy reductions of 13–63 GJ yr^{-1} across different climate zones, which is equal to 4–20 months of typical household electricity consumption, particularly benefiting hot regions (Fig. 3f).

Thermal and visual comfort

PRC materials have been envisioned as a promising strategy to mitigate the urban heat island (UHI) effect, but their large-scale urban adoptions remain challenging. While sky-facing horizontal surfaces (for example, roofs) can effectively maximize radiative cooling, vertical surfaces (for example, walls), which typically constitute ~70% of building exteriors, are less effective as they do not directly face outer space[8]. Additionally, super-white PRC materials exacerbate this issue as sunlight was trapped through multiple reflections between adjacent buildings (Extended Data Fig. 8a). This trapped sunlight is redirected towards the ground and pedestrians, potentially elevating the local microclimate and reducing both thermal and visual comfort (Fig. 4a and Supplementary Fig. 20).

To address these challenges, we conducted a microclimate simulation using the Princeton urban canopy model (Supplementary Note 8 and Supplementary Table 3)[23,24,56]. These simulations integrated PRC materials to evaluate their effects within typical urban canyon configurations, incorporating both shortwave (sunlight) and longwave (IR) radiative heat exchanges (Extended Data Fig. 8a). Surface temperatures of walls and ground, as well as MRT governing urban microclimate[57], were derived by solving the energy balance within the canyon. The results showed that while high-albedo surfaces reduce wall temperature, they increase ground temperature and MRT as a result of sunlight trapping, particularly in low-aspect-ratio canyons and indirect solar irradiation (Fig. 4b, Extended Data Fig. 8b–h and Supplementary Figs. 21–23). Such phenomenon is exacerbated by super-white PRC materials, heating the ground and reducing pedestrian thermal comfort. In contrast, PLACs

https://doi.org/10.1038/s41893-025-01657-y

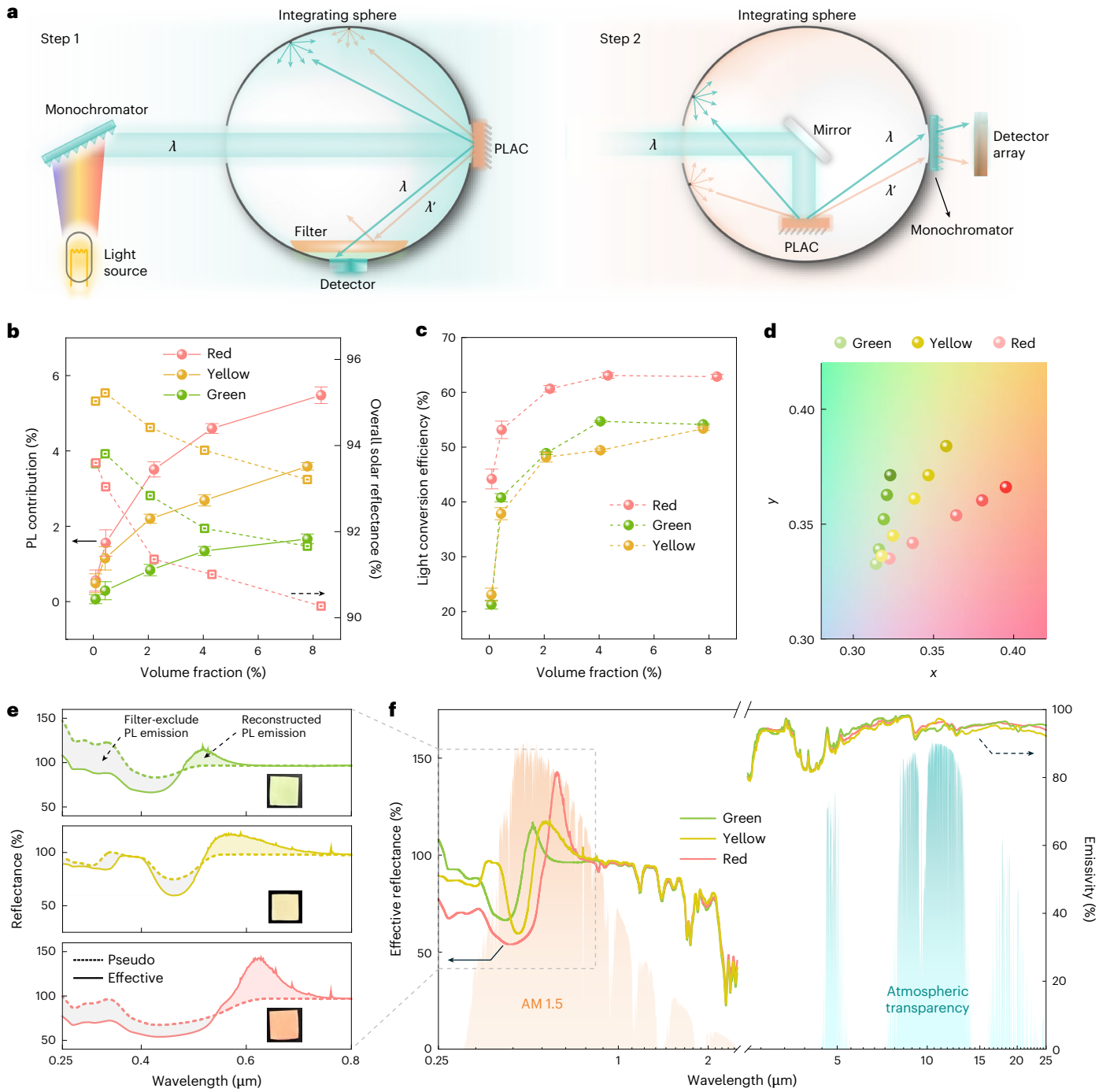

Fig. 2 | Optical and chromatic optimizations of PLACs. a, Schematic illustration of the proposed SFP method. Two steps are included as follows: step 1, decoupling the PL via short-pass filters to obtain exact spectral reflectance at the excitation wavelength region; and step 2, detailed PL characterization for reconstructing PL emission at the emission wavelength region. **b**, Overall solar reflectance and PL contribution as a function of the volume fraction of PL pigments. Measured from five independent PLACs per group. Bar heights, mean values; error bars, standard deviation ($n = 5$). Overall solar reflectance decreases with the increase in PL pigments since the imperfect light conversion inevitably induces thermal loads, while PL contribution to the overall solar reflectance rises with a decreasing slope at increasing volume fractions, indicating PL saturation at high concentrations. **c**, Light conversion efficiency as a function of the volume fraction of PL pigments. Measured from five independent PLACs per group. Bar height, mean values; error bars, standard deviation ($n = 5$). The light conversion efficiency increases rapidly at low-volume fractions but approaches a plateau at high-volume fractions. **d**, Chromaticity coordinates in the CIE 1931 colour space for PLACs with varying volume fractions for PL pigments as shown in **b** and **c**. The colour saturation increases with the volume fraction of PL pigments. **e**, Pseudo (dashed lines) and effective (solid lines) reflectance spectra in the UV–VIS ranges for green, yellow and red PLACs at the volume fractions for PL pigments of 7.8%, 7.8% and 8.3%, respectively. Insets are the images of the three PLACs. Effective reflectance reveals lower values at the excitation range and >100% reflectance at the emission range. The grey and green/yellow/red shaded regions denote the filter-decoupled regions and the reconstructed PL emissions, respectively. **f**, Effective solar reflectance and IR emissivity of PLACs as shown in **e**. The orange and cyan shaded regions indicate normalized solar irradiation and atmospheric transparency.

https://doi.org/10.1038/s41893-025-01657-y

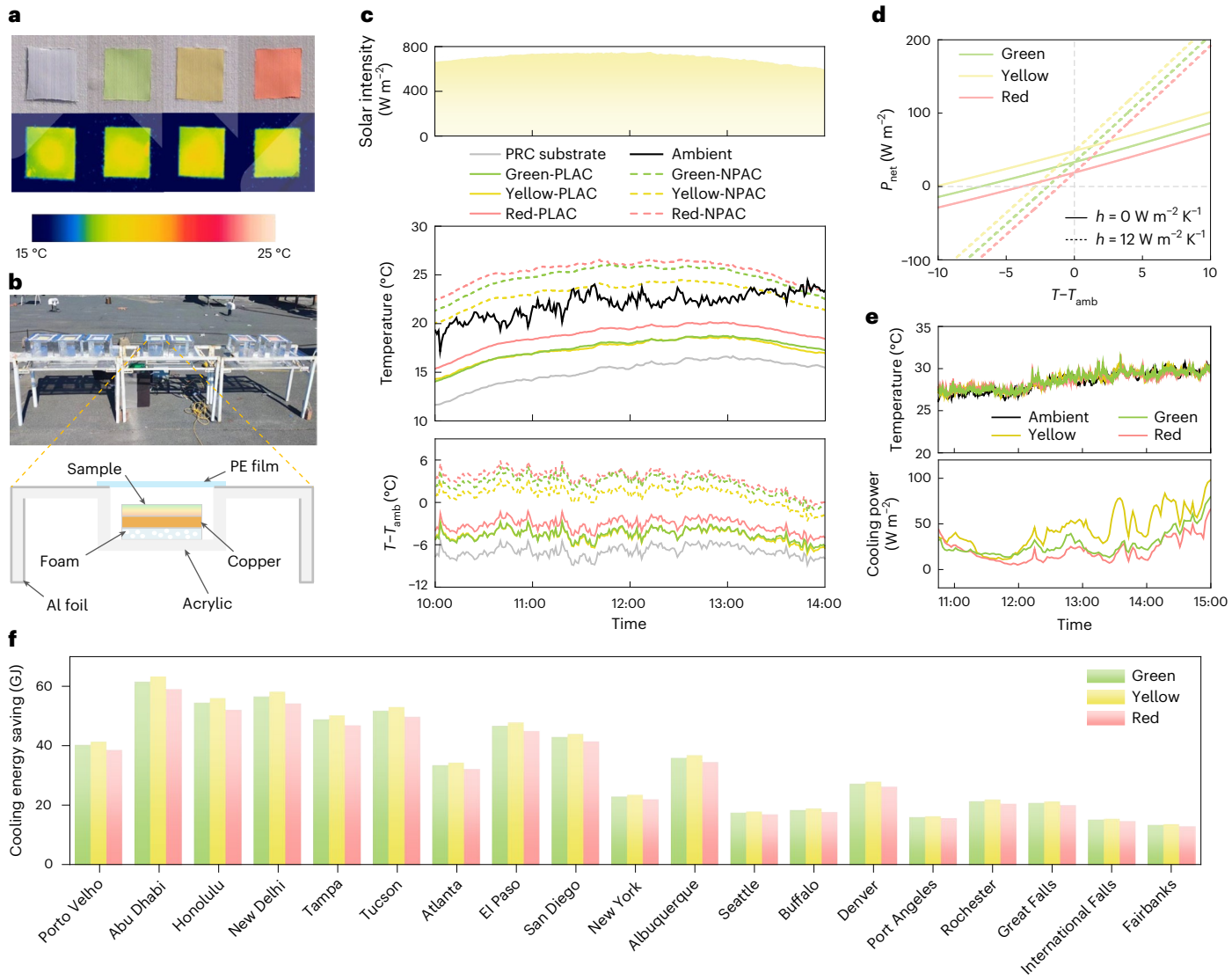

Fig. 3 | Cooling performance and energy-saving evaluation of PLACs. **a**, Photographs (top panel) and corresponding thermal images (bottom panel) of the PRC substrate and the three PLACs under sunlight. **b**, Photograph (top panel) and a schematic illustration (bottom panel) of the setup for outdoor field tests. **c**, Results of the outdoor field test during noontime, including solar intensity, sample temperature and temperature difference between the samples and the ambient air. The temperature of the PLACs was 3.7 °C, 3.9 °C and 2.2 °C lower than the ambient air and 7.2 °C, 6.1 °C and 7.8 °C lower than the NPACs for green, yellow and red, respectively, during noontime (11:00–13:00 on 3 October 2024 in Changchun, China) at peak sunlight of ~750 W m^{-2}. **d**, Theoretical calculation of the net cooling power of the three PLACs as a function of temperature difference. The green, yellow and red PLACs can achieve subambient temperature reductions of 6.9 °C, 10.2 °C and 3.8 °C at an ideal thermal insulation (h = 0 W m^{-2} K^{-1}, solid lines) and of 2.0 °C, 2.9 °C and 1.1 °C at insufficiency thermal insulation (h = 12 W m^{-2} K^{-1}, dashed lines), respectively. The theoretical net cooling power for green, yellow and red PLACs is 33.2 W m^{-2}, 48.5 W m^{-2} and 18.8 W m^{-2}, respectively. **e**, Cooling power measurements from the outdoor field test. The temperature of the three PLACs followed the ambient temperature as a result of the feedback-controlled heater under the PLACs. The measured cooling power for green, yellow and red PLACs was 28.1 W m^{-2}, 44.4 W m^{-2} and 20.1 W m^{-2}, respectively, matching well with the simulation results in **d**. **f**, Evaluation of annual cooling energy savings for the three PLACs. The selected 19 cities represent typical climate zones worldwide.

mitigate these issues (Fig. 4c) with MRT reduced by up to 9.3 °C and ground temperature lowered by 4.2 °C (Fig. 4d and Supplementary Fig. 24), primarily through reducing shortwave radiation. We then calculated the UTCI as a thermal comfort indicator to quantitatively assess people's perception of thermal stress (Supplementary Note 8 and Supplementary Table 4)[58,59]. As shown in Fig. 5e, the year-round TDP (UTCI > 26 °C) are reduced by 8.6% in climate zone 1A (very hot humid) when PLAC is used, highlighting its effectiveness in improving thermal comfort.

In addition to localized heat, canyon sunlight trapping also induces glare, which negatively impacts visual comfort. To assess this effect, we analysed the distribution of daylight intensity to intuitively visualize the influence of whiteness. A visual comfort index, DGP, was calculated to quantify glare perception, as it strongly correlated to illuminance (Supplementary Note 8, Supplementary Figs. 25 and 26 and Supplementary Table 5)[60,61]. Furthermore, the perceived colour appearance and brightness were derived to intuitively evaluate visual quality in urban canyons. As shown in Fig. 4f, Extended Data Fig. 9 and Supplementary Figs. 27 and 28, PLAC not only reduces daylight intensity on walls and outdoor glare but also enhances the perceived visual aesthetics, particularly under oblique sunlight. On a global scale (Fig. 5g), the year-round VDP (DGP > 0.35) are reduced by 5.8% in climate zone 0B (extremely hot dry) when PLAC is used. These simulation results, together with experimental validations (Supplementary Note 8 and Supplementary Fig. 29),

https://doi.org/10.1038/s41893-025-01657-y

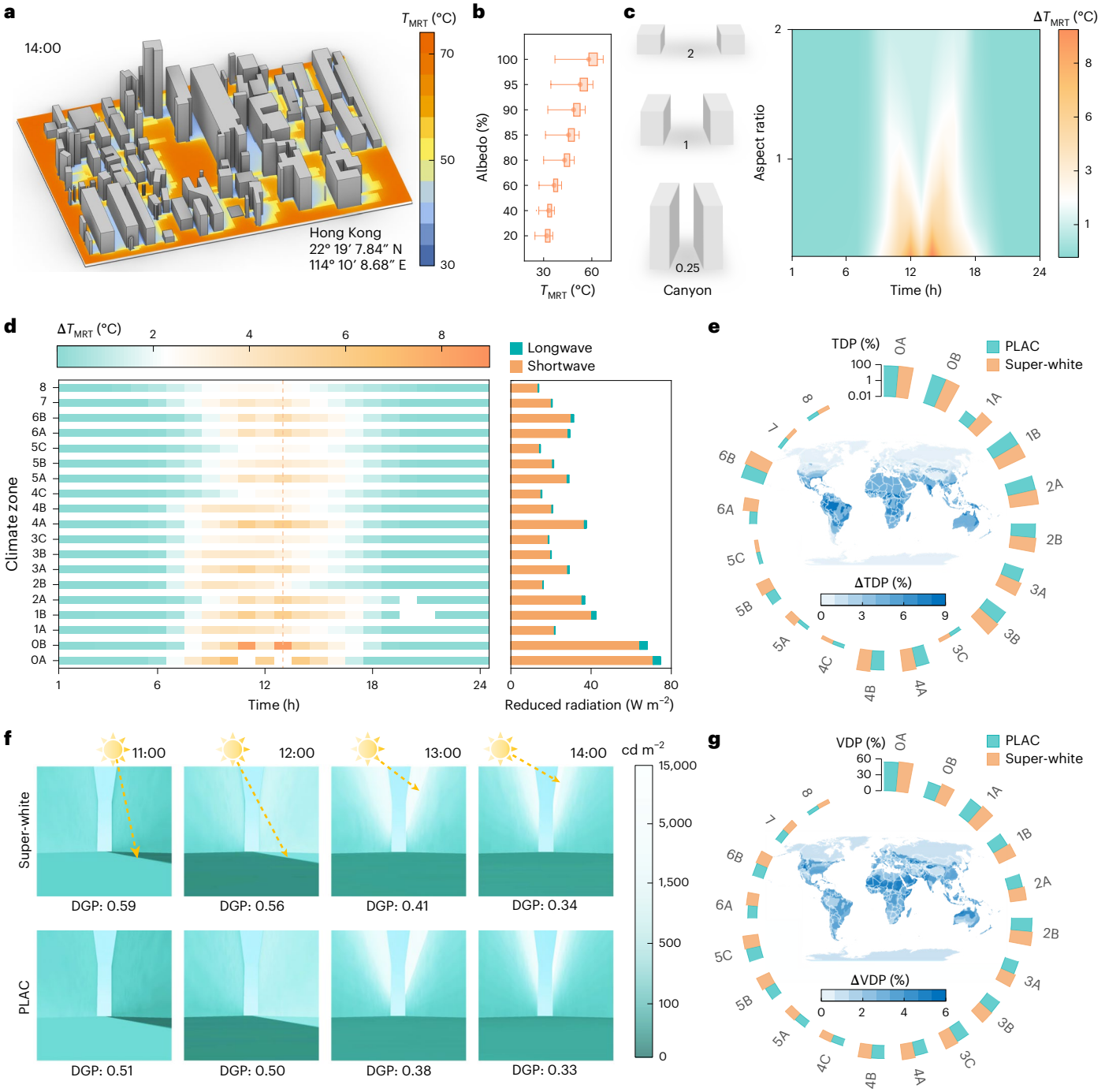

Fig. 4 | Urban thermal and glare evaluations of PLACs. a, Simulated MRT distribution at the height of 2 m over the urban area in Hong Kong. The surface albedo of building exteriors is set to 99.6%. **b**, MRT in typical urban canyons as a function of building exterior albedos. Dots, mean values (over 30 d); error bars, range (minimum to maximum values); boxes, distribution at 25–75%. **c**, Schematics of different canyon aspect ratios (left) and average 24-h MRT reduction through applying PLAC-based building exteriors. The canyon aspect ratios range from 0.25 to 2.00. PLACs can greatly reduce MRT compared with super-white PRCs for dense urban canyons during noontime. **d**, The 24-h MRT reduction for 19 typical climate zones on the global scale (left) and shortwave/longwave contribution to MRT reduction at 13:00 (right). PLAC-induced MRT reduction is predominantly due to the reduction of shortwave radiation. **e**, TDP for urban canyons with PLAC and super-white PRC as building exteriors. PLAC induces shorter TDP for all climate zones. Inset shows global mapping of TDP reduction (ΔTDP) via PLAC. **f**, False-colour images of daylight intensity distribution during noontime (from 11:00 to 14:00) for urban canyons with super-white PRC (top) and PLAC (bottom) as building exteriors. PLAC induces weaker daylight intensity and thereby results in a smaller DGP. The yellow arrows indicate the shadow edge at different times. **g**, VDP for urban canyons with PLAC and super-white PRC as building exteriors. PLAC also induces shorter VDP for all climate zones. Inset shows global mapping of VDP reduction (ΔVDP) via PLAC.

underscore that, while retaining the aesthetic and cooling benefits of PRC materials, the moderate whiteness of PLAC effectively mitigates sunlight trapping in urban canyons, thereby improving thermal and visual comfort. This balance enables PLAC to outperform recent coloured PRCs with comparable cooling performance (Supplementary Fig. 30 and Supplementary Tables 1 and 2), making it a superior alternative for addressing the challenges associated with urban deployments of PRC materials.

https://doi.org/10.1038/s41893-025-01657-y

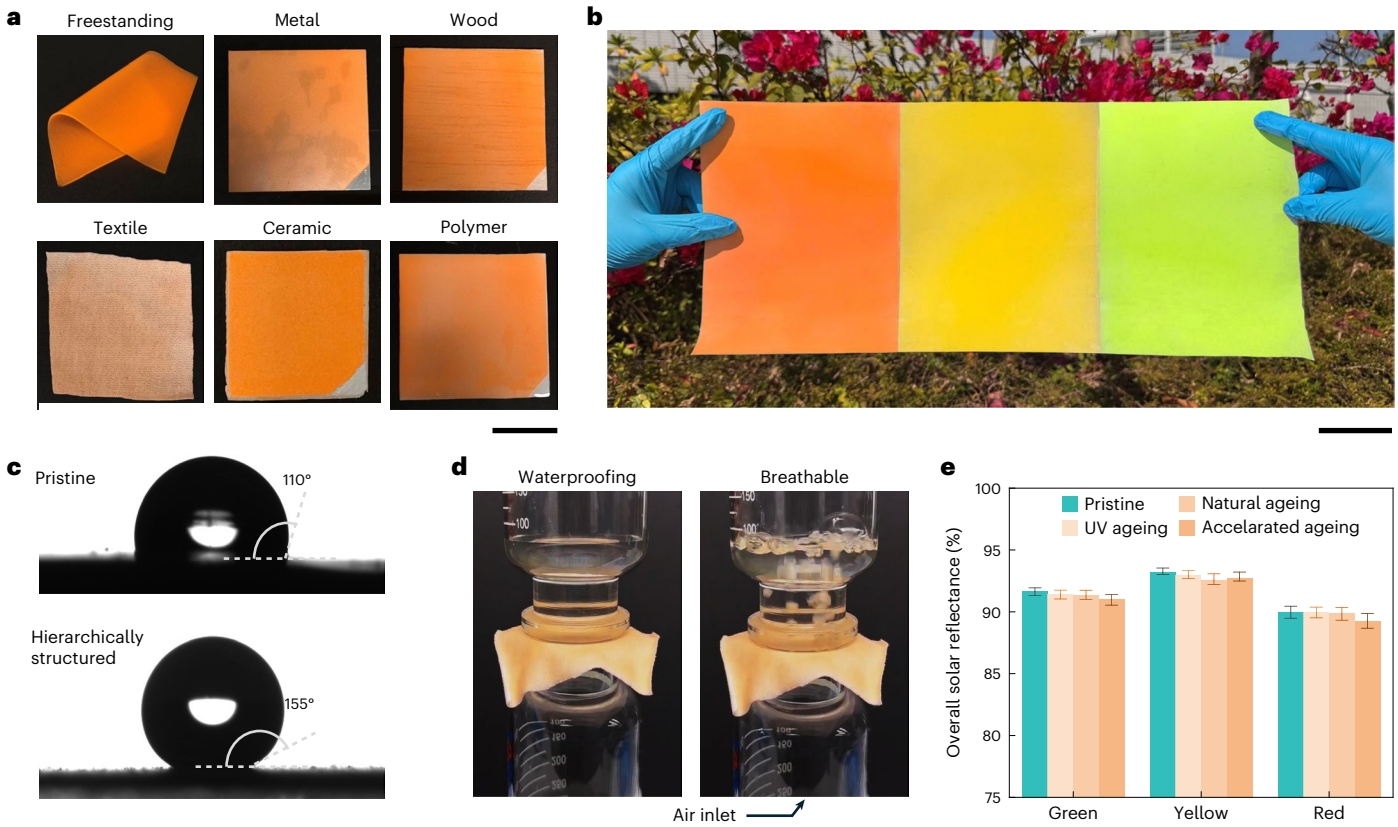

Fig. 5 | Functionalities and durability of PLACs. a, Photographs of a freestanding red PLAC and red PLACs on an aluminium plate, wood, cotton textile, ceramic and polymer substrates. **b**, A photograph of large-scale PLACs. **c**, Water contact angles for the as-prepared PLAC with moderate hydrophobicity (top) and the PLAC with a hierarchically structured surface revealing super-hydrophobicity (bottom). **d**, Photographs demonstrating the waterproofing effect (left) and breathability (right) of cotton textile spray coated with red PLAC. **e**, Overall solar reflectance of PLACs before and after a 5-month UV ageing, 1-month natural ageing and 300-h accelerated ageing. Measured from three independent PLACs per group. Bar heights, mean values ($n = 3$); error bars, range (minimum to maximum values). Scale bars, 2.5 cm (**a**), 10 cm (**b**).

Functionalities and durability

Beyond the cooling capacity and urban microclimate improvement, PLACs feature robust applicability. Our PLACs are coating-like flexible films that can be either freestanding or spin coated, blade coated and spray coated onto a variety of substrates, such as metal, wood, textile, cooling ceramics and polymers with good adhesion (Fig. 5a). This compatibility with different substrates is essential for expanding their applications from building exteriors to personal and electronic equipment. Scalable production of PLACs is also feasible, considering their large-scale urban applications (Fig. 5b). Moreover, the elastomeric matrix (PDMS) provides PLACs with excellent mechanical properties. By modifying elasticity during the polymerization process, freestanding PLACs undergo adjustable elastic and plastic deformations with Young's modulus varying from 0.2 MPa to 2 MPa (Extended Data Fig. 10a,b). This tenfold variation in ductility can also expand the applications of PLACs in flexible and stretchable forms, which is challenging for the inorganic counterparts of PRC[11,12].

Durability is an essential issue for long-term applications considering the complexity of environmental impacts including water, dust and UV light, especially for polymer-based composites that tend to degrade in both colour and cooling performance[11,62–65]. Hence, we engineered our PLACs with strengthened hydrophobic properties through a facile spray process, in which hierarchical aggregations of SiO_2 nanoparticles were formed on the surface. The as-prepared PLACs had a water contact angle of 110° due to the moderate hydrophobicity of the PDMS. After surface engineering through the spray process, the water contact angle increased to 155°, revealing super-hydrophobicity without influencing optical properties (Fig. 5c and Extended Data Fig. 10e). Therefore, dust can be removed instantly from their surface with water spray or natural rain, keeping the surface clean. Even without such surface engineering, spray-coated PLACs can make porous substrates, such as textiles, waterproof and breathable, which is combined with high flexibility, demonstrating their potential applications for personal thermal management (Fig. 5d, Extended Data Fig. 10c–d and Supplementary Video). Notably, our PLACs revealed excellent durability under UV irradiation of 5 months, natural outdoor exposure for 1 month and accelerating degradation tests for 300 h. Both optical and chromatic performance showed negligible degradation (Fig. 5e and Extended Data Fig. 10f–h). With this excellent durability, PLACs can provide stable cooling effects and urban benefits for various geographic and meteorological conditions, especially in hot and humid regions.

Discussion

We successfully developed a series of PLACs using photoluminescence to address the key challenge for urban skins, by combining aesthetic enhancement, cooling energy savings and urban environment improvement. By integrating synergistic optical, chromatic and thermal design principles, the produced PLACs demonstrate consistent subambient cooling performance for vivid green, yellow and red. Through quantitatively optimized light down-conversion, PLACs are able to reduce thermal loads and enhance cooling power, unlocking considerable energy-saving potential. By leveraging thermal and visual comfort metrics, we showed that the moderate whiteness of PLACs reduces sunlight trapping and improves urban microclimate. These cool colours break the traditional dependence on a monotonous white appearance in passive cooling materials, alleviating excessive visual and thermal

stress in urban environments and enhancing their practicality in combating the UHI effect. Furthermore, the coating-like PLACs feature facile fabrication, excellent flexibility and enhanced hydrophobicity and durability, ensuring their compatibility and long-term performance across diverse real-world applications. By reducing the reliance on energy-intensive air conditioning systems, PLACs directly contribute to lowering greenhouse gas emissions and mitigating climate change. Their ability to improve urban microclimates and reduce heat stress not only enhances urban livability but also supports public health in increasingly warming cities. Additionally, the scalable and durable nature of PLACs ensures minimal environmental impact during integration into existing infrastructure. These attributes highlight their potential for scalable deployment as urban skins, enabling sustainable urban development and energy solutions on a global scale. Beyond their immediate functionalities, the PLACs offer a means of energy transfer by converting absorbed light into re-emitted photons and new perspectives for thermal management, energy harvesting and energy transfer technologies. This work not only advances passive cooling technologies but also inspires concepts in multifunctional material design, paving the way for innovative solutions to address the pressing challenges of energy efficiency and environmental sustainability.

Methods

Preparation of PLACs, NPACs and PRC substrate

PLACs were fabricated as follows: 5 g of PDMS (Sylgard 184, Dow), 0.4 g of curing agent (Sylgard 184, Dow) and 2 ml of toluene (>99.5%, Sigma Aldrich) were added into a beaker and stirred by a magnetic stirrer at 800 rpm for 15 min to obtain a clear mixture. Then 0.5 g of SiO_2 nanoparticles (50 nm diameter, monodisperse, MiTaKe New Materials) and corresponding amounts of PL pigments (Shantou Dafeng Chem) (for different concentrations) were added into the mixture and further stirred at 1,000 rpm for 1 h to uniformly disperse the SiO_2 nanoparticles and PL pigments. After that, the suspension was placed in a vacuum oven at room temperature for 1 h to extract the air bubbles and toluene. The emulsion of PLAC was then obtained. For freestanding PLAC, the PLAC emulsion was poured into an aluminium mould with customized size and depth, followed by ventilation oven curing at 80 °C for 2 h. Then, a soft film was peeled off as freestanding PLAC. For PLACs on substrates such as PDMS-Al_2O_3 PRC, metal, wood, ceramic and polymer, the PLAC emulsion was poured onto the substrate, followed by spin/blade coating processes and ventilation oven curing at 80 °C for 2 h. For PLACs on textiles, the suspension was directly poured into a spray gun without vacuum treatment and spray coated onto the textile, followed by ventilation oven curing at 80 °C for 2 h. NPACs followed the same fabrication processes as PLACs but using commercial pigments (iron oxide pigments, Xinghui Chemical).

For mechanical property measurements, the PLACs were fabricated at the PDMS:curing agent ratio of 10:1, 15:1 and 20:1. Other components kept the same ratio with PDMS as above. The size was confined as $53 \times 13 \times 1\ mm^3$ for measurements.

The PDMS-Al_2O_3 PRC substrate was fabricated as follows: 5 g of PDMS, 0.4 g of curing agent, 2 ml of toluene and 5 g of Al_2O_3 nanoparticles (MSE Supplies) were added into a beaker and stirred by a magnetic stirrer at 1,000 rpm for 1 h, followed by vacuum treatment of 1 h. The white emulsion was then poured into an aluminium mold and cured in a ventilation oven at 80 °C for 2 h.

Characterizations of PLACs

A commercial UV–VIS–NIR spectrometer (Lambda 1050+ equipped with an integrating sphere, PerkinElmer) was used. The pseudo spectral reflectance at solar spectrum (0.25–2.5 μm) was directly measured by the UV–VIS–NIR spectrometer following common procedure. Short-pass filters (GU Optics) with different cut-off wavelengths for different PL pigments, together with an ultra-white filter holder (cooling ceramic with an overall solar reflectance of 99.6%), were placed before the detector in the integrating sphere (Extended Data Fig. 3b). The exact reflectance was measured via correction of the filters. The angular-resolved spectral reflectance was measured using a Cary 5000 UV–VIS–NIR spectrometer (Agilent) equipped with an integrating sphere (DRA 2500) and an angle-adjustable transmission bracket. The IR emissivity (2.5–25 μm) was measured by a Fourier transform IR spectrometer (Nicolet iS50 with an integrating sphere, Thermo Fisher Scientific).

The PL properties of the phosphor powders and the PLACs were characterized by an Edinburgh Instruments FLS1000 Photoluminescence Spectrometer following the standard procedure for excitation/emission spectra and following the procedure in Extended Data Fig. 3c for measuring the absolute absorption and photoluminescence quantum yield (PLQY) at varying excitation wavelengths. Supplementary Fig. 4f–h shows typical data for PLQY measurements of PLACs. During each quantum yield test, a specific excitation wavelength (λ) within the excitation range of the PL pigments was selected as the incident wavelength. The line-width of this excitation is typically 5–10 nm, limited by the resolution of the equipment. The detection range was then set to cover both the incident excitation and emission regions (typically from 20 nm shorter than λ to the end of the emission range), ensuring that all the excitation and emission photons were effectively collected.

The micromorphology of PL pigments and cross-section of PLACs were characterized by an FEI Quanta 450 field-emission scanning electron microscope. The X-ray diffraction was measured by a D2 PHASE XE-T X-ray Diffraction System (Bruker). The mechanical properties including strain–stress curves and Young's modulus were obtained using an Instron 5942 Micro Newton Tester under a stretching speed of 10 mm min^{-1}. The UV degradation was carried out in a UV ageing test chamber (Dongguan Rongzheng Yida Electronic Tech, RZ-KUV400A) with a 40-W UVA-340 lamp based on ASTM-154 (standard practice for operating fluorescent UV lamp apparatus for exposure of non-metallic materials). Standard accelerating degradation test for 300 h was conducted using a Ci5000 Xenon lamp artificial weathering tester (L3112) as well as a coating stain resistance flushing device (L1083), following the guidelines of GB/T 9755-2014. These tests simulated the combined effects of environmental stressors by including exposure to UV radiation (340 nm) with an intensity of 0.51 W m^{-2}, relative humidity of 50 ± 10%, black mark temperature of 65 ± 2 °C, air temperature inside the test chamber of 38 ± 3 °C and a rainfall cycle at 18 min of rain followed by 102 min without rain. Additional tests involved airborne pollutant spraying and flushing to mimic real-world conditions. Natural outdoor exposure of PLACs was also conducted on a rooftop for 1 month.

Scattering and absorption analysis

The scattering and absorption efficiencies for SiO_2 nanoparticles in Fig. 1d were calculated using Mie theory for spherical particles. The normalized electric field |E| at 0.25 μm and electromagnetic loss density |Q| at 8.5 μm were simulated using COMSOL Multiphysics. PDMS was applied as the surrounding dielectric medium for both cases.

Outdoor field tests

The cooling performance was evaluated in outdoor field tests in Changchun (2–4 October 2024) and Hong Kong (18–20 January 2025). An acrylic box ($25 \times 25 \times 15\ cm^3$) was covered with aluminium foil to avoid solar heating and placed ~50 cm above the ground to minimize ground heating. The PLAC-PRCs were attached to a copper plate using thermally conductive tape and placed on plastic foam in the acrylic box. Thermocouples (TT-K-30, K type, Kaipusen) were placed between the sample and the thermally conductive tape to measure the real-time sample temperature, which was collected by a data logger (multi-channel data logger GL840, GRAPHTECH). The weather conditions, including ambient air temperature, sunlight intensity, humidity

and wind speed, were recorded through a mini weather station (YG-BX, YIGU). For cooling power measurement, the field test was conducted in Hong Kong on 7 November 2024. A resistance-based flexible heater was attached to the bottom of the copper plate for each sample. The heater was connected to a DC power supply which was adjusted substantially so that the temperature of the sample followed the ambient air temperature. The output electric power of the power supply was recorded as the cooling power.

Energy-saving simulations

The energy-saving simulation was conducted using EnergyPlus v.22.1.0. A typical building developed by the Pacific Northwest National Laboratory of the US Department of Energy, that is, a four-story mid-rise apartment with the floor dimension of 46 m (152 ft, length) × 17 m (55.5 ft, width) × 3 m (10 ft, height), was used as the prototype to simulate the whole building energy consumption (Extended Data Fig. 7a)[66,67]. The model follows application building codes and standards for energy efficiency requirements, including typical operation/occupancy schedules, lighting/miscellaneous loads and HVAC systems. The building energy-saving performances in Extended Data Fig. 7b were obtained by calculating the difference in energy consumption for cooling usage between two types of building surfaces, that is, PLACs and the default building surface in the prototype (baseline). While for the PL-induced building energy-saving potential (Extended Data Fig. 7c), the baseline was simulated with the exact solar reflectance of the same PLACs. The locations for simulation cover typical climate zones around the world including[55]: Porto Velho (Zone 0A, extremely hot humid), Abu Dhabi (Zone 0B, extremely hot dry), Honolulu (Zone 1A, very hot humid), New Delhi (Zone 1B, very hot dry), Tampa (Zone 2A, hot humid), Tucson (Zone 2B, hot dry), Atlanta (Zone 3A, warm humid), El Paso (Zone 3B, warm dry), San Diego (Zone 3C, warm marine), New York (Zone 4A, mixed humid), Albuquerque (Zone 4B, mixed dry), Seattle (Zone 4C, mixed marine), Buffalo (Zone 5A, cool humid), Denver (Zone 5B, cool dry), Port Angeles (Zone 5C, cool marine), Rochester (Zone 6A, cold humid), Great Falls (Zone 6B, cold dry), International Falls (Zone 7, very cold) and Fairbanks (Zone 8, subarctic/Arctic).

Superhydrophobic engineering

To enhance hydrophobicity, top superhydrophobic coating was applied at the surface of PLACs, consisting of similar components of PLACs and can be fabricated through a facile spray-coating process. The coating emulsion was prepared as follows: 0.5 g of PDMS, 40 mg of curing agent, 10 ml of toluene and 50 mg of tetraethyl orthosilicate (98%, Sigma Aldrich) were mixed and ultrasonicated for 15 min. Both 50 mg of hydrophilic and hydrophobic SiO_2 nanoparticles (50 nm, MiTaKe New Materials) were then added into the solution and ultrasonicated for 30 min. The mixture was poured into the spray gun and sprayed at the PLACs for 30 s. The hydrophilic nanoparticles cannot dissolve in the solution and thereby agglomerate because of the hydroxyl group on the surface. Although the hydrophobic nanoparticles cannot directly connect to the hydroxyl group, the adhesive PDMS molecular chains can help connect the hydrophobic nanoparticles and the hydrophilic agglomeration, forming a hierarchically structured surface after spraying onto the PLACs[68]. After curing by ventilation oven at 60 °C for 1 h, the superhydrophobic coating was formed on the surfaces of PLACs, enabling a water contact angle of ~155°.

Reporting summary

Further information on research design is available in the Nature Research Reporting Summary linked to this article.

Data availability

The data that support the findings of this study are available from the corresponding authors upon request. Source data are provided with this paper.

Code availability

The code for the urban thermal and visual comfort model can be made available upon request.

References

1. *The Green Cooling Initiative* (United Nations, 2012).
2. Sachar, S., Campbell, I. & Kalanki, A. *Solving the Global Cooling Challenge: How to Counter the Climate Threat from Room Air Conditioners* (Rocky Mountain Institute, 2018).
3. Raman, A. P., Anoma, M. A., Zhu, L., Rephaeli, E. & Fan, S. Passive radiative cooling below ambient air temperature under direct sunlight. *Nature* **515**, 540–544 (2014).
4. Yin, X., Yang, R., Tan, G. & Fan, S. Terrestrial radiative cooling: using the cold universe as a renewable and sustainable energy source. *Science* **370**, 786–791 (2020).
5. Zhai, Y. et al. Scalable-manufactured randomized glass–polymer hybrid metamaterial for daytime radiative cooling. *Science* **355**, 1062–1066 (2017).
6. Mandal, J. et al. Hierarchically porous polymer coatings for highly efficient passive daytime radiative cooling. *Science* **362**, 315–319 (2018).
7. Li, T. et al. A radiative cooling structural material. *Science* **364**, 760–763 (2019).
8. Xie, F. et al. Subambient daytime radiative cooling of vertical surfaces. *Science* **386**, 788–794 (2024).
9. Fan, S. & Li, W. Photonics and thermodynamics concepts in radiative cooling. *Nat. Photonics* **16**, 182–190 (2022).
10. Stephens, G., Campbell, G. & Haar, T. V. Earth radiation budgets. *J. Geophys. Res. Oceans* **86**, 9739–9760 (1981).
11. Zhao, X. et al. A solution-processed radiative cooling glass. *Science* **382**, 684–691 (2023).
12. Lin, K. et al. Hierarchically structured passive radiative cooling ceramic with high solar reflectivity. *Science* **382**, 691–697 (2023).
13. Hsu, P.-C. et al. Radiative human body cooling by nanoporous polyethylene textile. *Science* **353**, 1019–1023 (2016).
14. Zeng, S. et al. Hierarchical-morphology metafabric for scalable passive daytime radiative cooling. *Science* **373**, 692–696 (2021).
15. Wu, R. et al. Spectrally engineered textile for radiative cooling against urban heat islands. *Science* **384**, 1203–1212 (2024).
16. Haechler, I. et al. Exploiting radiative cooling for uninterrupted 24-hour water harvesting from the atmosphere. *Sci. Adv.* **7**, eabf3978 (2021).
17. Raman, A. P., Li, W. & Fan, S. Generating light from darkness. *Joule* **3**, 2679–2686 (2019).
18. Zhao, D. et al. Development of a single-phase thermosiphon for cold collection and storage of radiative cooling. *Appl. Energy* **205**, 1260–1269 (2017).
19. *Radiative Cooling Technology Market Size and Forecast* (Verified Market Research, 2024).
20. *HVAC System Market* (Markets and Markets, 2024).
21. Falasca, S. et al. High albedo materials to counteract heat waves in cities: An assessment of meteorology, buildings energy needs and pedestrian thermal comfort. *Build. Environ.* **163**, 106242 (2019).
22. Portella, A. *Visual Pollution: Advertising, Signage and Environmental Quality* (Routledge, 2016).
23. Pigliautile, I., Pisello, A. & Bou-Zeid, E. Humans in the city: representing outdoor thermal comfort in urban canopy models. *Renew. Sustain. Energy Rev.* **133**, 110103 (2020).
24. Huang, X., Bou-Zeid, E., Pigliautile, I., Pisello, A. L. & Mandal, J. Optimizing retro-reflective surfaces to untrap radiation and cool cities. *Nat. Cities* **1**, 275–285 (2024).
25. Merritt, F. S. *Building Design and Construction Handbook* (McGraw-Hill, 2001).

26. Marshall, S. G., Jackson, H. O. & Stanley, M. S. *Individuality in Clothing Selection and Personal Appearance* (Pearson, 2011).
27. Ranscombe, C., Hicks, B., Mullineux, G. & Singh, B. Visually decomposing vehicle images: Exploring the influence of different aesthetic features on consumer perception of brand. *Des. Stud.* **33**, 319–341 (2012).
28. Dunne, A. *Hertzian Tales: Electronic Products, Aesthetic Experience, and Critical Design* (MIT Press, 2008).
29. Li, W., Shi, Y., Chen, Z. & Fan, S. Photonic thermal management of coloured objects. *Nat. Commun.* **9**, 4240 (2018).
30. Xi, W., Liu, Y., Zhao, W., Hu, R. & Luo, X. Colored radiative cooling: how to balance color display and radiative cooling performance. *Int. J. Therm. Sci.* **170**, 107172 (2021).
31. Yu, S., Zhang, Q., Wang, Y., Lv, Y. & Ma, R. Photonic-structure colored radiative coolers for daytime subambient cooling. *Nano Lett.* **22**, 4925–4932 (2022).
32. Zhu, W. et al. Structurally colored radiative cooling cellulosic films. *Adv. Sci.* **9**, 2202061 (2022).
33. Kim, H. H., Im, E. & Lee, S. Colloidal photonic assemblies for colorful radiative cooling. *Langmuir* **36**, 6589–6596 (2020).
34. Min, S., Jeon, S., Yun, K. & Shin, J. All-color sub-ambient radiative cooling based on photoluminescence. *ACS Photonics* **9**, 1196–1205 (2022).
35. Yalçın, R. A., Blandre, E., Joulain, K. & Drévillon, J. Colored radiative cooling coatings with fluorescence. *J. Photonics Energy* **11**, 032104–032104 (2021).
36. Xu, J. et al. Colored radiative cooling coatings using phosphor dyes. *Mater. Today Nano* **19**, 100239 (2022).
37. Ma, X. et al. Fluorescence-enabled colored bilayer subambient radiative cooling coatings. *Adv. Opt. Mater.* **12**, 2303296 (2024).
38. Wang, X. et al. Sub-ambient full-color passive radiative cooling under sunlight based on efficient quantum-dot photoluminescence. *Sci. Bull.* **67**, 1874–1881 (2022).
39. Ma, X. et al. Fluorescence-enhanced light-blue bilayer radiative cooling coatings. *J. Mater. Chem. A* **12**, 20921–20926 (2024).
40. Spalding, M., Ravilious, C. & Green, E. P. *World Atlas of Coral Reefs* (Univ. California Press, 2001).
41. Brown, B. Coral bleaching: causes and consequences. *Coral Reefs* **16**, S129–S138 (1997).
42. Salih, A., Larkum, A., Cox, G., Kühl, M. & Hoegh-Guldberg, O. Fluorescent pigments in corals are photoprotective. *Nature* **408**, 850–853 (2000).
43. Dove, S., Hoegh-Guldberg, O. & Ranganathan, S. Major colour patterns of reef-building corals are due to a family of GFP-like proteins. *Coral Reefs* **19**, 197–204 (2001).
44. Salih, A. et al. The role of host-based color and fluorescent pigments in photoprotection and in reducing bleaching stress in corals. In *Proc. 10th Int. Coral Reef Symp*. 746–756 (International Society for Reef Studies, Japanese Coral Reef Society, 2006).
45. Huang, G. et al. Radiative cooling and indoor light management enabled by a transparent and self-cleaning polymer-based metamaterial. *Nat. Commun.* **15**, 3798 (2024).
46. Zhou, L. et al. Sustainable and inexpensive polydimethylsiloxane sponges for daytime radiative cooling. *Adv. Sci.* **8**, 2102502 (2021).
47. Chen, Y. et al. Colored and paintable bilayer coatings with high solar-infrared reflectance for efficient cooling. *Sci. Adv.* **6**, eaaz5413 (2020).
48. Young, A. T. Rayleigh scattering. *Appl. Opt.* **20**, 533–535 (1981).
49. Ding, Z. et al. Designer SiO_2 metasurfaces for efficient passive radiative cooling. *Adv. Mater. Interfaces* **11**, 2300603 (2024).
50. Abou-Hamdan, L. et al. Transition from phononic to geometrical Mie modes measured in single subwavelength polar dielectric spheres. *ACS Photonics* **9**, 2295–2303 (2022).
51. Ma, X. et al. Effects of Stokes shift and Purcell enhancement on fluorescence-assisted radiative cooling. *J. Mater. Chem. A* **10**, 19635–19640 (2022).
52. Levinson, R., Chen, S., Ferrari, C., Berdahl, P. & Slack, J. Methods and instrumentation to measure the effective solar reflectance of fluorescent cool surfaces. *Energy Build.* **152**, 752–765 (2017).
53. Xue, X. et al. Creating an eco-friendly building coating with smart subambient radiative cooling. *Adv. Mater.* **32**, 1906751 (2020).
54. Ma, J.-W. et al. A photoluminescent hydrogen-bonded biomass aerogel for sustainable radiative cooling. *Science* **385**, 68–74 (2024).
55. Edition, S. et al. *Energy Standard for Buildings Except Low-rise Residential Buildings* (ASHRAE, 2010).
56. Wang, Z. H., Bou-Zeid, E. & Smith, J. A. A coupled energy transport and hydrological model for urban canopies evaluated using a wireless sensor network. *Q. J. R. Meteorol. Soc.* **139**, 1643–1657 (2013).
57. *ASHRAE Handbook—Fundamentals* (ASHRAE, 2001).
58. Błażejczyk, K. et al. An introduction to the universal thermal climate index (UTCI). *Geogr. Pol.* **86**, 5–10 (2013).
59. Jendritzky, G., De Dear, R. & Havenith, G. UTCI—why another thermal index?. *Int. J. Biometeorol.* **56**, 421–428 (2012).
60. Wienold, J. & Christoffersen, J. Evaluation methods and development of a new glare prediction model for daylight environments with the use of CCD cameras. *Energy Build.* **38**, 743–757 (2006).
61. Wienold, J. Dynamic daylight glare evaluation. In *11th Int. IBPSA Conference* 944–951 (IBPSA Publications, 2009).
62. Song, J. et al. Durable radiative cooling against environmental aging. *Nat. Commun.* **13**, 4805 (2022).
63. Göpferich, A. Mechanisms of polymer degradation and erosion. *Biomaterials* **17**, 103–114 (1996).
64. Andrady, A. L., Hamid, S., Hu, X. & Torikai, A. Effects of increased solar ultraviolet radiation on materials. *J. Photochem. Photobiol. B* **46**, 96–103 (1998).
65. Bretz, S. E. & Akbari, H. Long-term performance of high-albedo roof coatings. *Energy Build.* **25**, 159–167 (1997).
66. Deru, M. et al. *US Department of Energy Commercial Reference Building Models of the National Building Stock* (National Renewable Energy Laboratory, 2011).
67. Goel, S. et al. *Enhancements to ASHRAE Standard 90.1 Prototype Building Models* (Pacific Northwest National Laboratory, 2014).
68. Gong, X. & He, S. Highly durable superhydrophobic polydimethylsiloxane/silica nanocomposite surfaces with good self-cleaning ability. *ACS Omega* **5**, 4100–4108 (2020).

Acknowledgements

This work was supported by Hong Kong Research Grant Council via General Research Fund project 11200923 (to C.Y.T.) and Research Fellow Scheme with reference no. RFS2425-1S06 (to C.Y.T.), as well as by the Innovation and Technology Commission via Innovation and Technology Fund project ITS/128/22FP (to C.Y.T.). This work was also supported by City University of Hong Kong for the project 'Fostering Innovation for Resilience and Sustainable Transformation', officially endorsed by the United Nations Educational, Scientific and Cultural Organization under the International Decade of Sciences for Sustainable Development (2024–2033) via the internal City University of Hong Kong account of 9610739 (to C.Y.T.). In addition, this work was also supported by a donation for a research project grant at City University of Hong Kong from i2Cool Limited, under project account no. 9220161 (to C.Y.T.). Furthermore, support was provided by National Natural Science Foundation of China (grant nos. 2525033, 62134009 and 62121005 to W.L.) and the International Partnership Program of Chinese Academy of Sciences or Future Network (grant no. 171GJHZ2023038FN to W.L.).

Author contributions

Conceptualization: Y.F., A.P., C.Y.T. Methodology: Y.F., C.W., K.L., A.P., Z.L., Y.Z. Investigation: Y.F., X.M., X.-W.Z., Z.L., X.C., X.L., W.W., C.T.K., Y.-H.Z., X.X., X.Z., W.L., C.Y.T. Funding acquisition: W.L., C.Y.T. Supervision: W.L., C.Y.T. Writing—original draft: Y.F., C.Y.T. Writing—review and editing: K.L., A.P., A.L.R., L.L., W.L., C.Y.T.

Competing interests

The authors declare no competing interests.

Additional information

Extended data is available for this paper at https://doi.org/10.1038/s41893-025-01657-y.

Supplementary information The online version contains supplementary material available at https://doi.org/10.1038/s41893-025-01657-y.

Correspondence and requests for materials should be addressed to Wei Li or Chi Yan Tso.

Peer review information *Nature Sustainability* thanks Young Min Song, Peng Xue, Hai-Bo Zhao and the other, anonymous, reviewer(s) for their contribution to the peer review of this work. Peer reviewer reports are available.

[1]School of Energy and Environment, City University of Hong Kong, Hong Kong SAR, China. [2]Department of Materials Science and Engineering, City University of Hong Kong, Hong Kong SAR, China. [3]GPL Photonics Laboratory, State Key Laboratory of Luminescence Science and Technology, Changchun Institute of Optics, Fine Mechanics and Physics, Chinese Academy of Sciences, Changchun, China. [4]China Southwest Architectural Design and Research Institute Co. Ltd., Chengdu, China. [5]Centre for Functional Photonics (CFP), City University of Hong Kong, Hong Kong SAR, China. ✉e-mail: weili1@ciomp.ac.cn; chiytso@cityu.edu.hk

https://doi.org/10.1038/s41893-025-01657-y

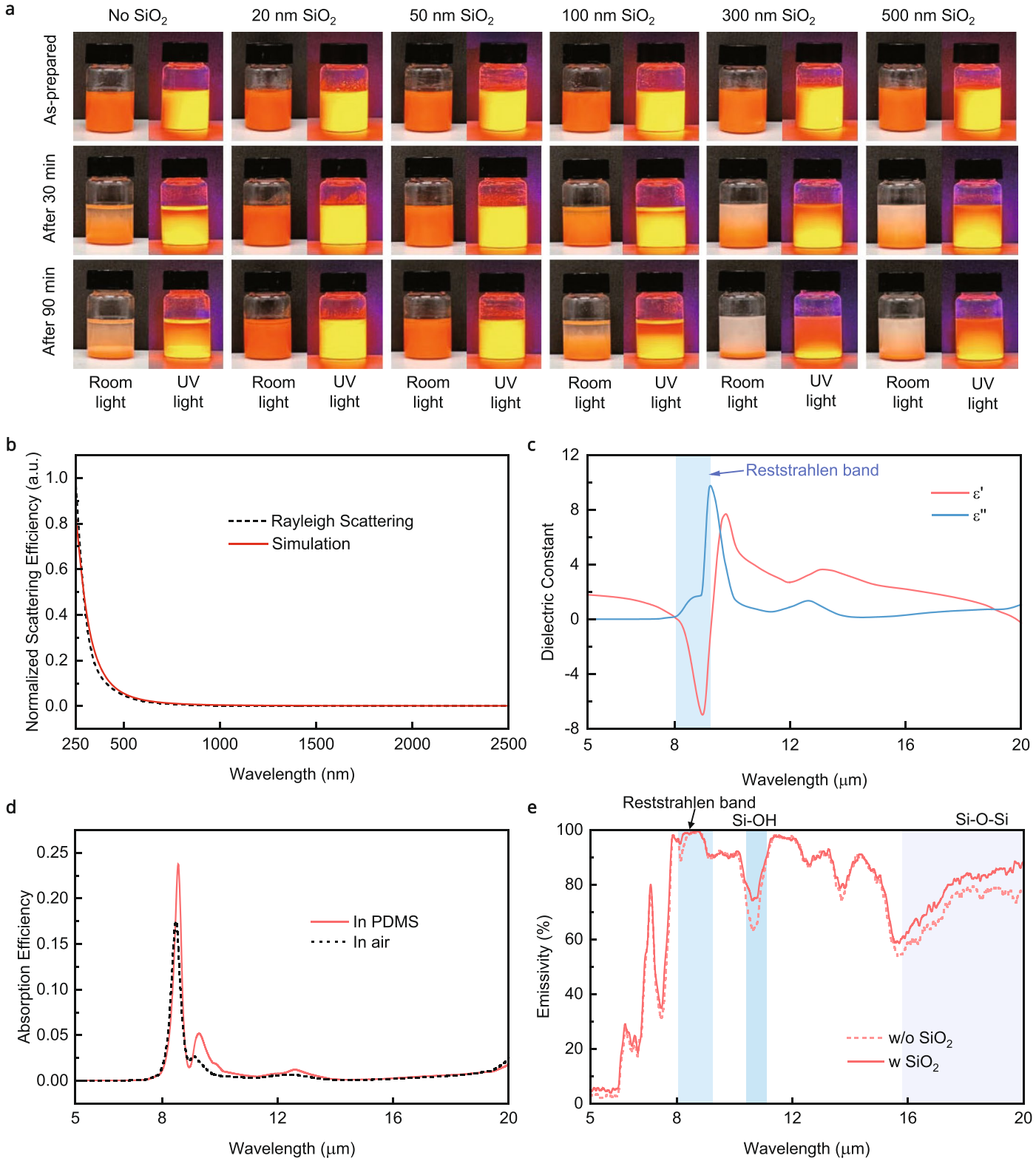

Extended Data Fig. 1 | Steric hindrance and optical contribution of SiO_2 nanoparticles. a, Photographs of PDMS-PL pigments solutions with and without different nano-sized SiO_2. **b**, Simulated scattering efficiency of a SiO_2 nanoparticle with a diameter of 50 nm, which well matches with the calculation result based on Rayleigh scattering. **c**, Dielectric constant of SiO_2 as a function of wavelength. Its real part (ε') shows negative values near 8.55 μm, which is known as the Reststrahlen band. **d**, Absorption efficiency of a SiO_2 nanoparticle with a diameter of 50 nm in PDMS (red line) and in air (dashed black line). Higher peak values can be obtained for PDMS as its impedance matches with SiO_2. **e**, Infrared emissivity for a 30 μm-thick PDMS with (solid line) and without (dashed line) SiO_2 nanoparticles. Emissivity enhancement can be observed for several wavelength regions.

https://doi.org/10.1038/s41893-025-01657-y

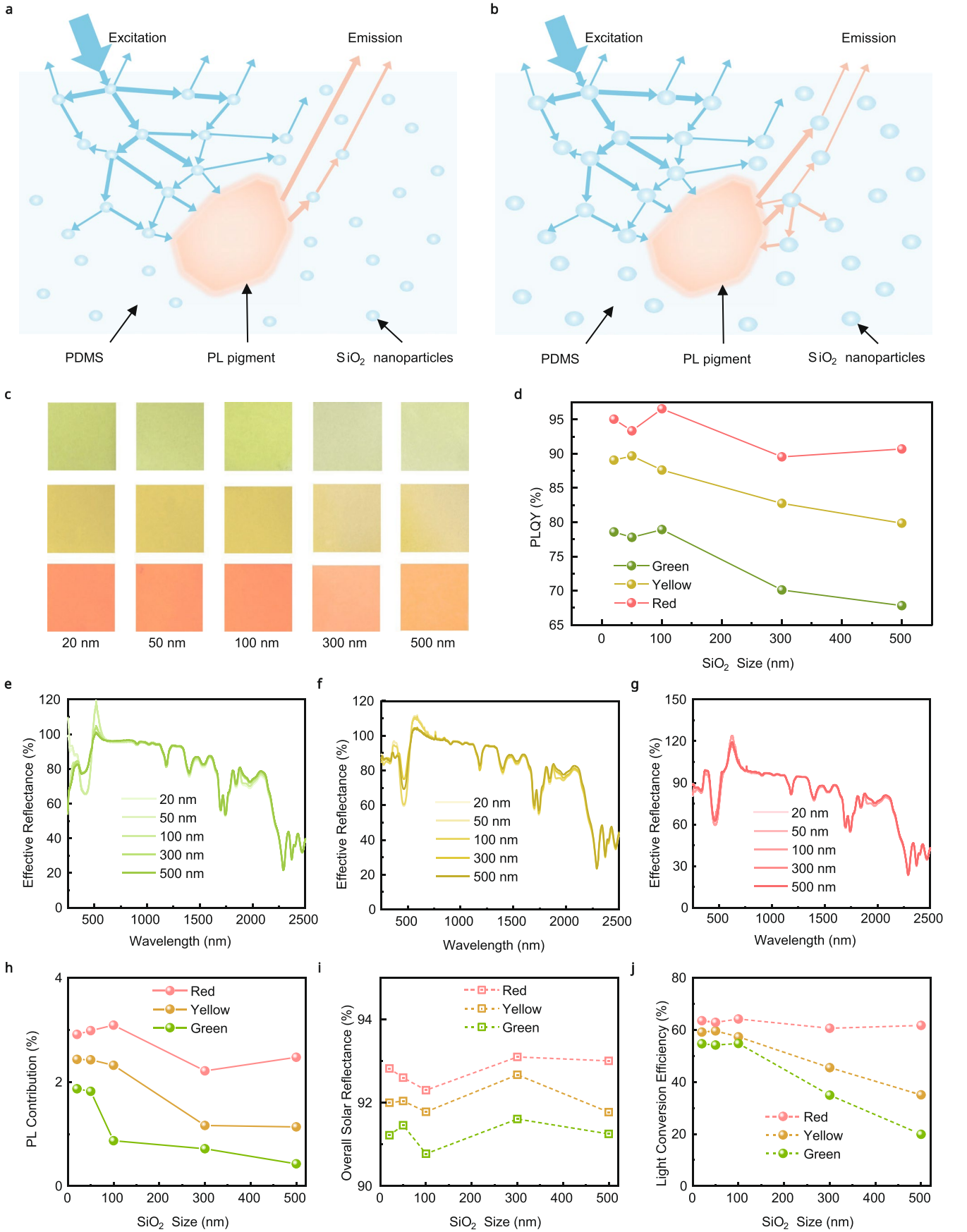

Extended Data Fig. 2 | See next page for caption.

https://doi.org/10.1038/s41893-025-01657-y

Extended Data Fig. 2 | Size effect of SiO_2 nanoparticles. a-b, Schematic illustrations of the light scattering processes for both excitation and emission light with smaller (**a**) and larger (**b**) SiO_2 particles. For both sizes, short-wavelength excitation light is directed toward the PL pigments, while larger SiO_2 particles scatter the emission light, leading to increased re-absorption. **c**, Photographs of green, yellow, and red PLACs with varying-sized SiO_2 nanoparticles. **d**, PLQYs of PLACs in (**c**). The excitation wavelengths are 400 nm, 460 nm, and 400 nm for green, yellow, and red PLACs, respectively. **e-g**, Effective spectral reflectance of green (**e**), yellow (**f**), and red PLACs (**g**) in (**c**). **h-j**, Corresponding PL contribution (**h**), overall solar reflectance (**i**), and light conversion efficiency (**j**) of PLACs.

https://doi.org/10.1038/s41893-025-01657-y

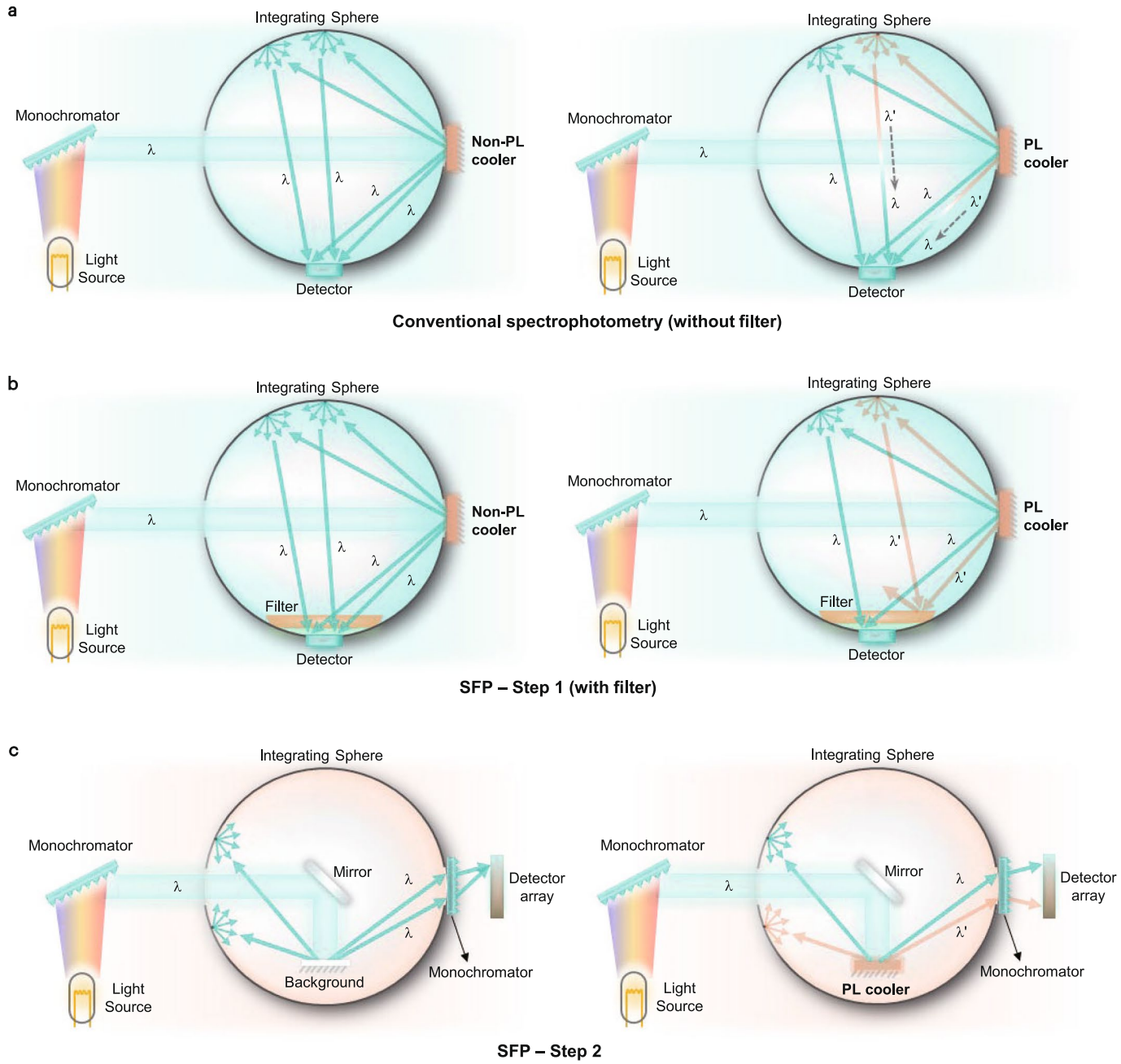

Extended Data Fig. 3 | Schematic illustrations of the light paths in conventional spectrophotometry and SFP method. a, Light paths in conventional UV-VIS-NIR spectrophotometry for non-PL (left) and PL coolers (right). This configuration works for non-PL coolers as all the reflected light (at the wavelength of λ) is correctly collected by the detector. While for PL coolers, both reflected light (at the wavelength of λ) and re-emitted light (at the wavelength of λ') are redirected to the detector. Due to the lack of monochromators in the integrating sphere, the re-emitted light will be misinterpreted as having the same wavelength as the reflected light (that is, λ) by the detector, resulting in misinterpretation of the contribution of PL emissions. **b**, Light paths in Step 1 of SFP method for non-PL (left) and PL coolers (right). For non-PL coolers, this configuration works similarly to conventional spectrophotometry. While for PL coolers, the added filter will reject re-emitted light (at the wavelength of λ'). Only reflected light (at the wavelength of λ) will be collected by the detector, leading to exact spectral reflectance. **c**, Light paths in Step 2 of SFP method. The background photon numbers are measured (left) as reference, followed by the measurement of PL coolers (right). Either reflected light or re-emitted light will be correctly collected by the detector array at corresponding wavelengths.

https://doi.org/10.1038/s41893-025-01657-y

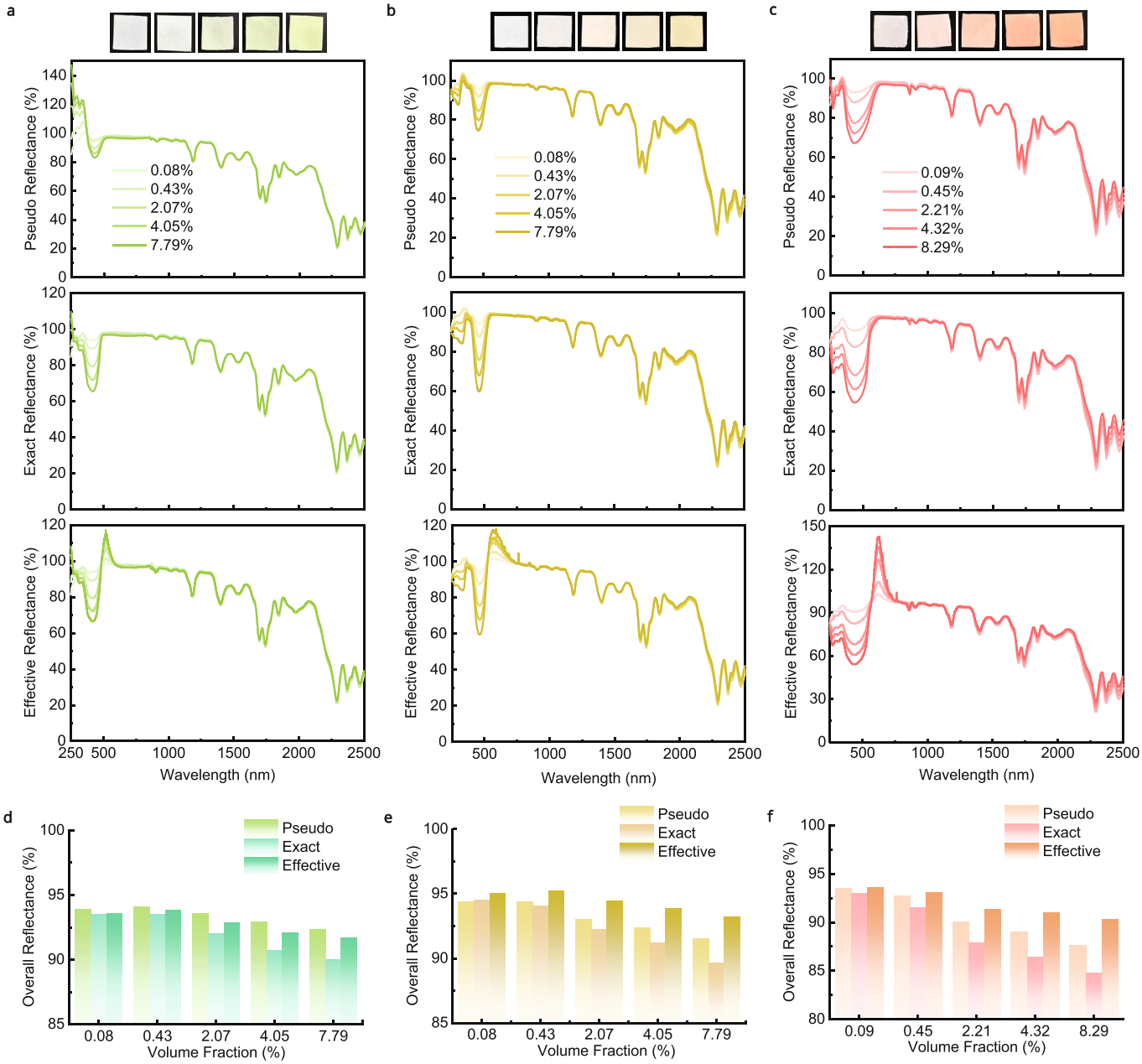

Extended Data Fig. 4 | Influences of volume fractions on optical properties. a-c, Photographs and pseudo (top), exact (middle), and effective (bottom) spectral reflectance of green (**a**), yellow (**b**), and red (**c**) PLACs with varying volume fractions of PL pigments. **d-f**, Overall solar reflectance for green (**d**), yellow (**e**), and red (**f**) PLACs, calculated from (**a-c**).

https://doi.org/10.1038/s41893-025-01657-y

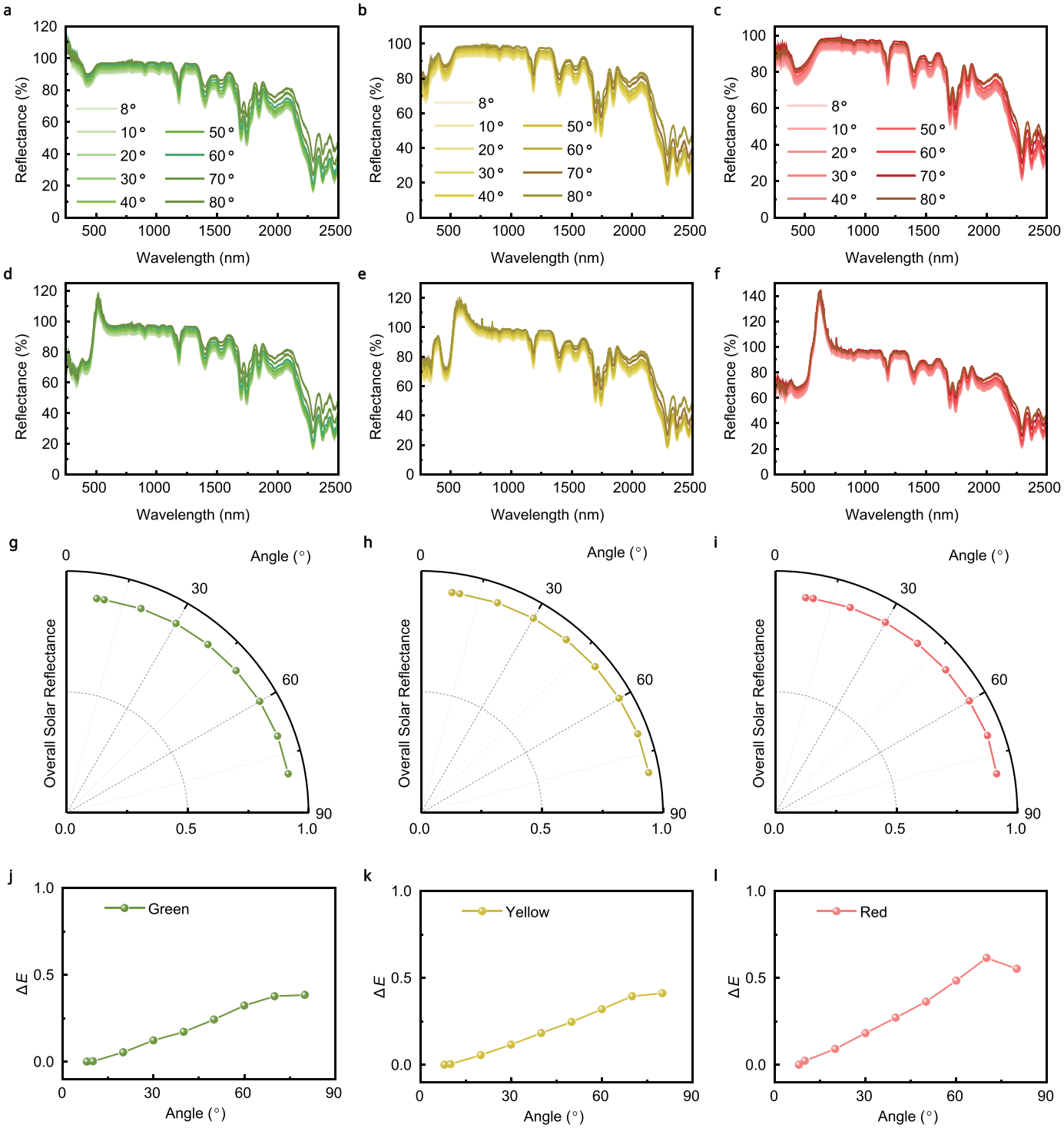

Extended Data Fig. 5 | Angular insensitivity of PLACs. a-c, Pseudo spectral reflectance of green (**a**), yellow (**b**), and red PLACs (**c**) under varying incident angles. **d-f**, Exact spectral reflectance of the PLACs in (**a-c**) under varying incident angles. **g-i**, Corresponding overall solar reflectance of the PLACs under varying incident angles. **j-l**, Corresponding color differences for green (**a**), yellow (**b**), and red PLACs (**c**) under varying incident angles.

https://doi.org/10.1038/s41893-025-01657-y

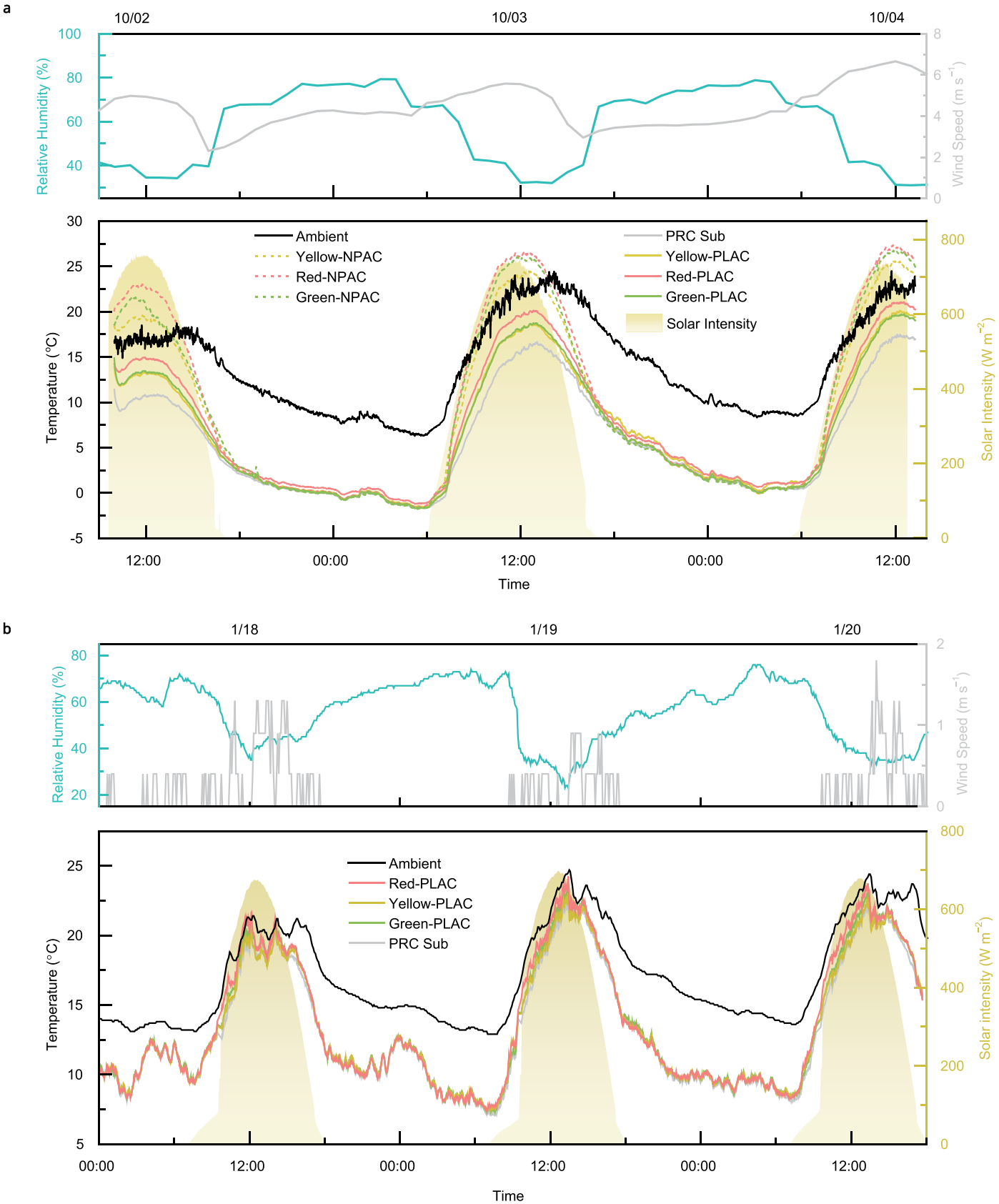

Extended Data Fig. 6 | Outdoor field test results for PLACs and NPACs. **a-b**, Recorded weather conditions (top) and temperature (bottom) for 3-day outdoor field test in Changchun, China (October 2-4, 2024) (**a**) and in Hong Kong, China (January 18-20, 2025) (**b**). Continuous subambient cooling effects can be observed in both cases. In (**b**), the subambient temperature reduction (averaged from 10:00 to 14:00 for 3 days) for white substrate, green, yellow, and red PLACs is 2.4, 1.7, 2.1, and 1.1 °C, respectively.

https://doi.org/10.1038/s41893-025-01657-y

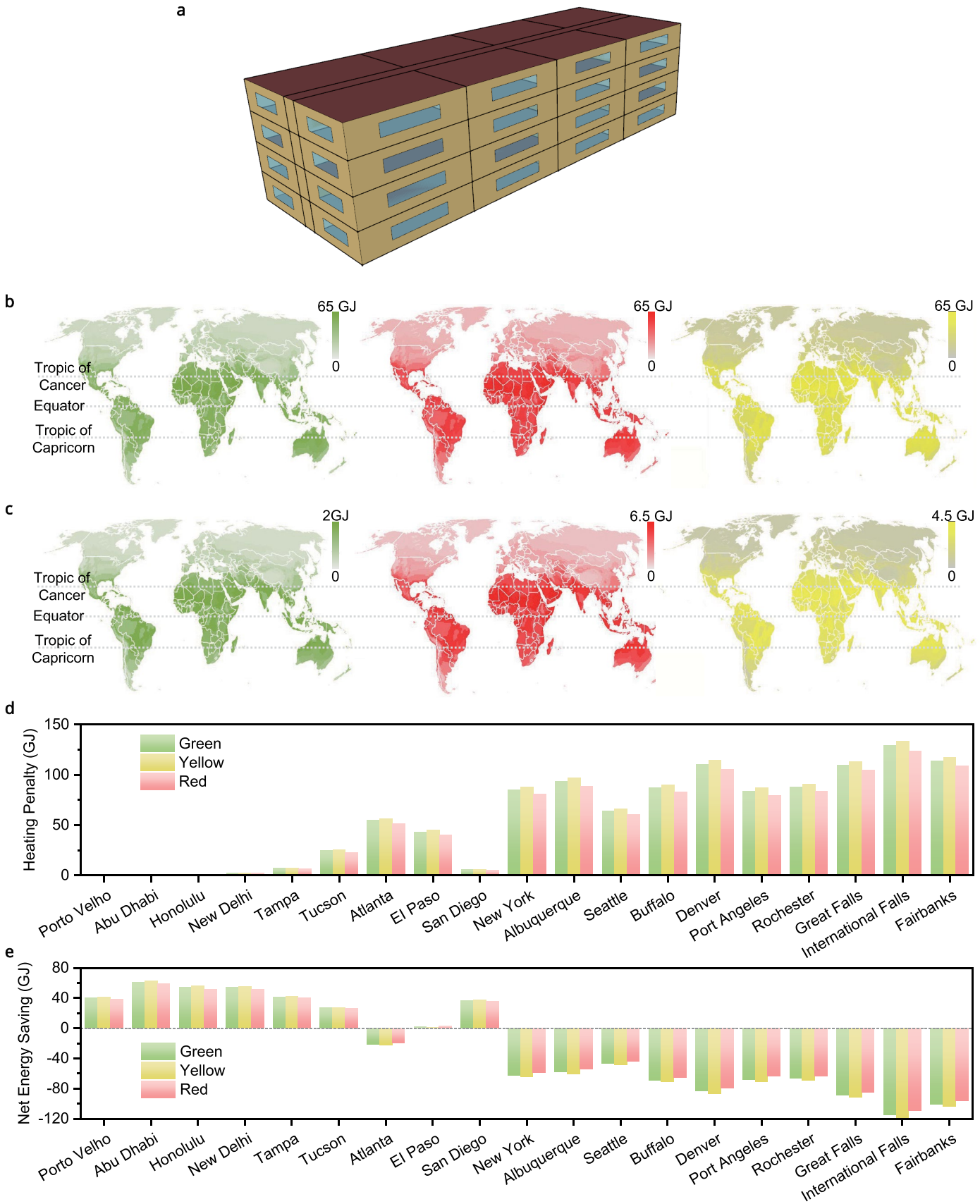

Extended Data Fig. 7 | Energy saving simulations. a, Building model for energy saving simulations. **b**, Simulated annual cooling energy saving for green (left), red (middle), and yellow (right) PLACs. **c**, Cooling energy saved from PL emissions for three PLACs. **d-e**, Evaluation of annual heating penalty (**d**) and annual net energy saving (**e**) for the three PLACs.

https://doi.org/10.1038/s41893-025-01657-y

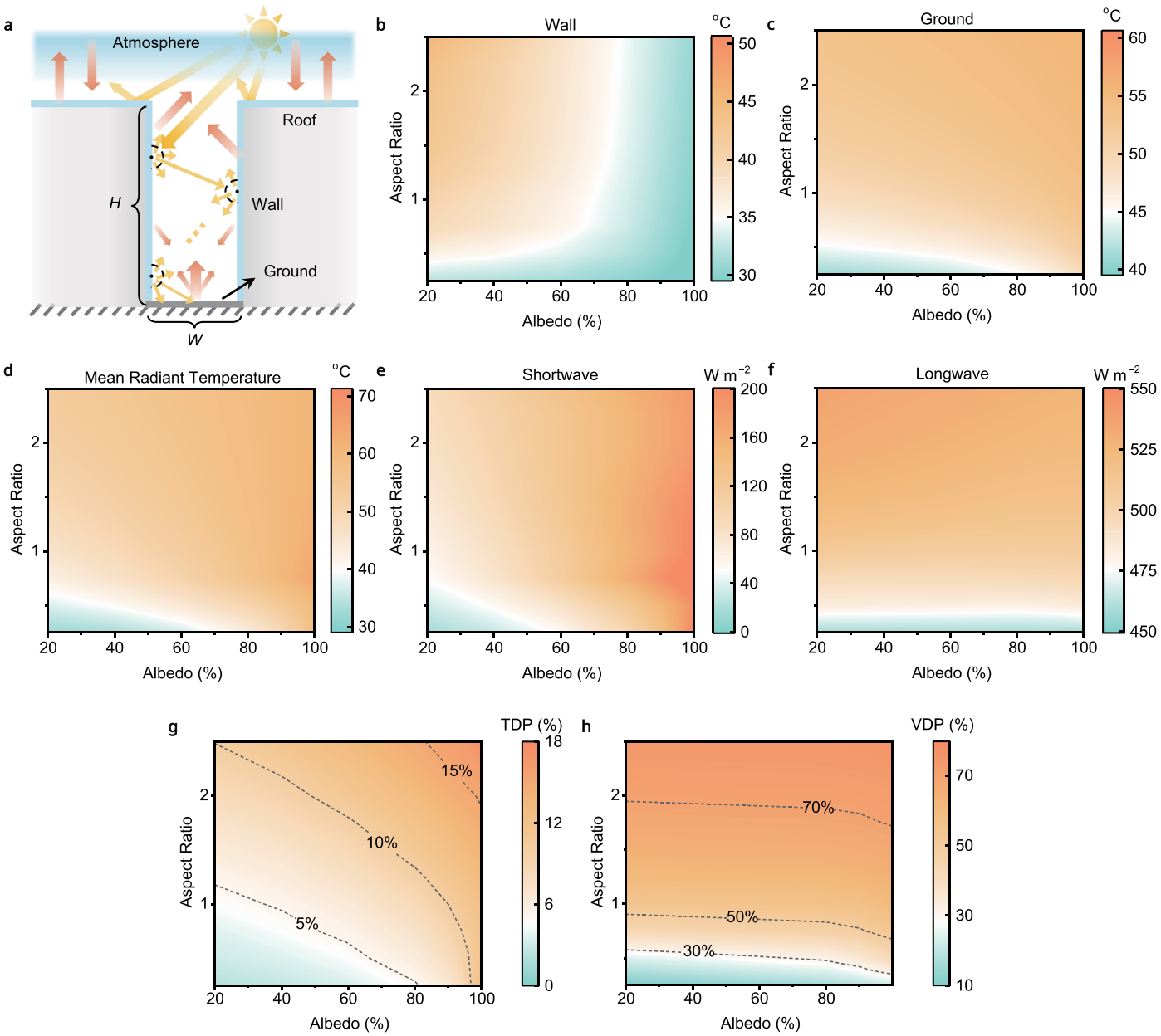

Extended Data Fig. 8 | Urban canyon simulation results. a, Schematic of 2D urban canyon configurations and corresponding radiative heat fluxes for PUCM simulations. Diffusive reflection/absorption was considered for walls and ground. Multiple reflection for shortwave/longwave radiation was included to obtain surface temperature and corresponding radiative heat fluxes. The aspect ratio of urban canyon is defined as *W*/*H*. **b-d**, Simulated temperature (maximum values in daytime, averaged over 1 month) of walls (**b**), ground (**c**), and MRT (**d**) with varying surface albedos of walls and aspect ratio of urban canyons. The wall temperature is lower with high albedos and small aspect ratios, while ground and MRT are higher with high albedos and large aspect ratios. **e-f**, Shortwave (**e**) and longwave (**f**) contribution of the MRT in (**d**). The increase of MRT at high albedos is predominantly due to the shortwave radiation. **g-h**, TDP (**g**) and VDP (**h**) with varying urban parameters (albedo and aspect ratio). The dashed lines denote the thresholds for different levels of thermal/visual comfort.

https://doi.org/10.1038/s41893-025-01657-y

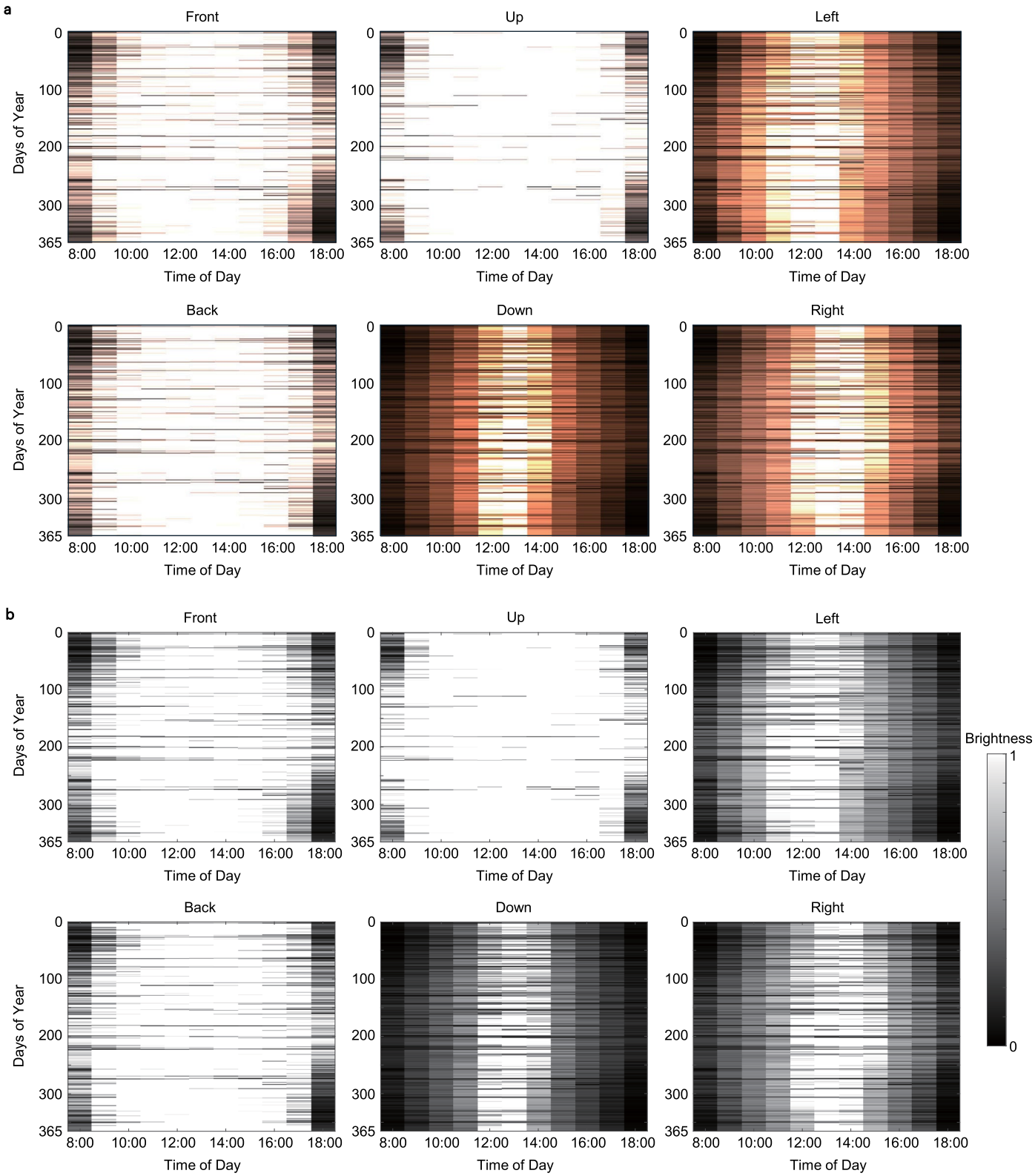

Extended Data Fig. 9 | Perceived color appearance and brightness in a PLAC-based urban canyon. a, Perceived color of pedestrians in a PLAC-based urban canyon throughout the year under varying viewing directions (front, back, up, down, left, and right). **b**, Corresponding brightness perceived by pedestrians in a PLAC-based urban canyon under varying viewing directions.

https://doi.org/10.1038/s41893-025-01657-y

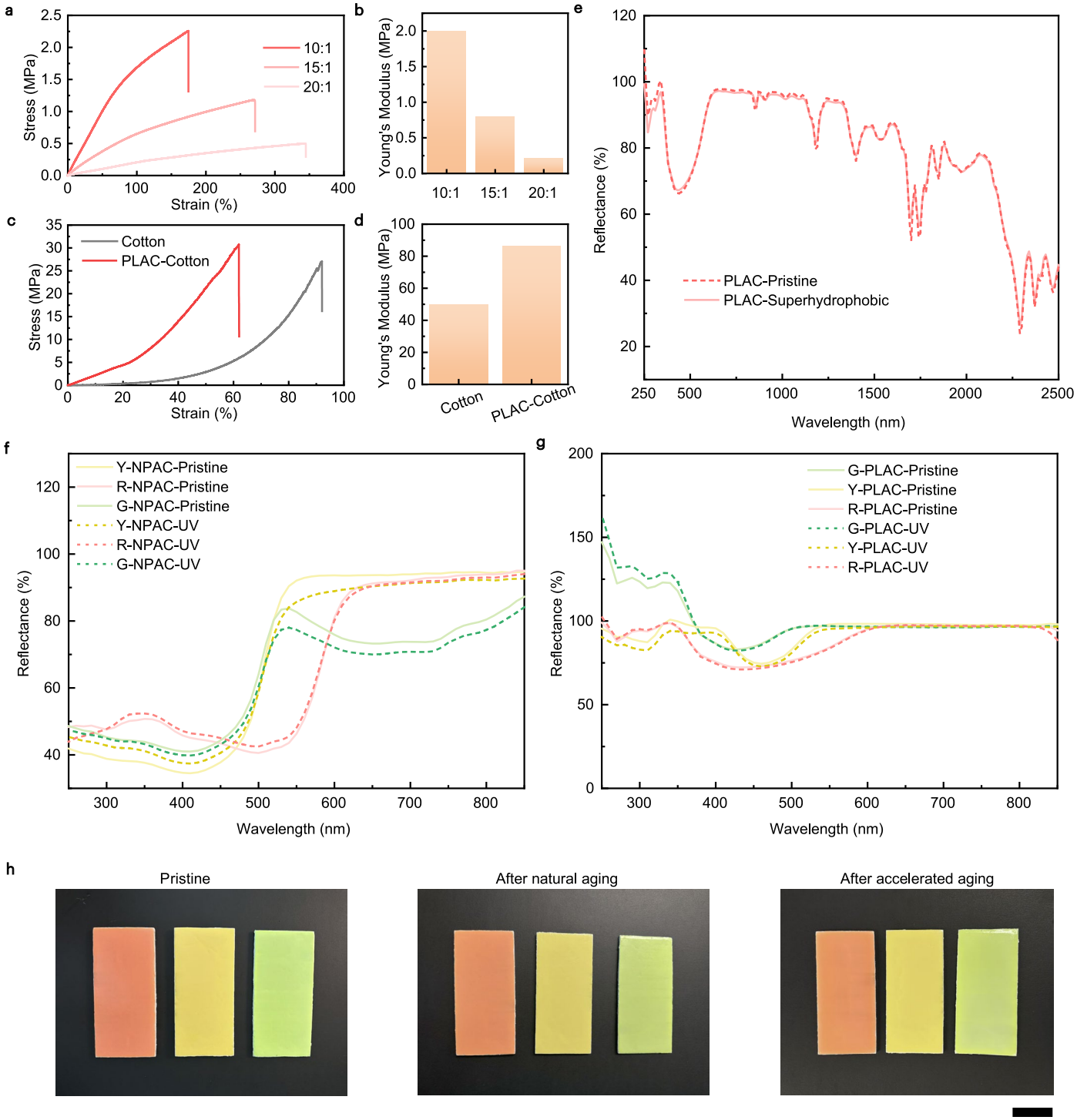

Extended Data Fig. 10 | Stability and flexibility of PLACs. a, Strain-stress curves for PLACs polymerized with different weight ratios between PDMS and curing agent. **b**, Young's modulus of three samples in (**a**). **c**, Strain-stress curves for cotton textiles with and without spray-coating of PLACs. **d**, Young's modulus of the two samples in (**c**). **e**, Spectral reflectance of PLACs before and after superhydrophobic surface engineering. **f-g**, Spectral reflectance of NAPCs (**f**) and PLACs (**g**) before and after UV irradiation for 5 months. **h**, Photographs of green, yellow, and red PLACs before aging and after natural/accelerated aging. Scale bar: 5 cm.

nature portfolio

Corresponding author(s): Chi Yan Tso, Wei Li

Last updated by author(s): Aug 20, 2025

Reporting Summary

Nature Portfolio wishes to improve the reproducibility of the work that we publish. This form provides structure for consistency and transparency in reporting. For further information on Nature Portfolio policies, see our Editorial Policies and the Editorial Policy Checklist.

Statistics

For all statistical analyses, confirm that the following items are present in the figure legend, table legend, main text, or Methods section.

n/a	Confirmed	
☐	☒	The exact sample size (*n*) for each experimental group/condition, given as a discrete number and unit of measurement
☐	☒	A statement on whether measurements were taken from distinct samples or whether the same sample was measured repeatedly
☒	☐	The statistical test(s) used AND whether they are one- or two-sided *Only common tests should be described solely by name; describe more complex techniques in the Methods section.*
☒	☐	A description of all covariates tested
☒	☐	A description of any assumptions or corrections, such as tests of normality and adjustment for multiple comparisons
☐	☒	A full description of the statistical parameters including central tendency (e.g. means) or other basic estimates (e.g. regression coefficient) AND variation (e.g. standard deviation) or associated estimates of uncertainty (e.g. confidence intervals)
☒	☐	For null hypothesis testing, the test statistic (e.g. *F*, *t*, *r*) with confidence intervals, effect sizes, degrees of freedom and *P* value noted *Give P values as exact values whenever suitable.*
☒	☐	For Bayesian analysis, information on the choice of priors and Markov chain Monte Carlo settings
☒	☐	For hierarchical and complex designs, identification of the appropriate level for tests and full reporting of outcomes
☒	☐	Estimates of effect sizes (e.g. Cohen's *d*, Pearson's *r*), indicating how they were calculated

Our web collection on statistics for biologists contains articles on many of the points above.

Software and code

Policy information about availability of computer code

Data collection	To calculate the temperature of urban skins, we have utilized a customized MATLAB (version: 2023a) code integrating Princeton Urban Canopy Model (PUCM) with radiative cooling. Detailed equations and calculation conditions are given in Supplementary Materials. To obtain the scattering and absorption properties of SiO2 nanoparticles, we have used the commercial software, COMSOL Multiphysics (version: 6.0), for numerical simulation. To predict the energy saving potential, we have employed an open source software, EnergyPlus (version: 22.2.0), to calculate the energy consumption.
Data analysis	We have used customized MATLAB (version: 2023a) codes for analyzing the spectral reflectance.

For manuscripts utilizing custom algorithms or software that are central to the research but not yet described in published literature, software must be made available to editors and reviewers. We strongly encourage code deposition in a community repository (e.g. GitHub). See the Nature Portfolio guidelines for submitting code & software for further information.

Data

Policy information about availability of data

All manuscripts must include a data availability statement. This statement should provide the following information, where applicable:

- Accession codes, unique identifiers, or web links for publicly available datasets
- A description of any restrictions on data availability
- For clinical datasets or third party data, please ensure that the statement adheres to our policy

The data that supports the findings of this study are available from the corresponding authors upon request.

Research involving human participants, their data, or biological material

Policy information about studies with human participants or human data. See also policy information about sex, gender (identity/presentation), and sexual orientation and race, ethnicity and racism.

Reporting on sex and gender	N/A
Reporting on race, ethnicity, or other socially relevant groupings	N/A
Population characteristics	N/A
Recruitment	N/A
Ethics oversight	N/A

Note that full information on the approval of the study protocol must also be provided in the manuscript.

Field-specific reporting

Please select the one below that is the best fit for your research. If you are not sure, read the appropriate sections before making your selection.

☐ Life sciences ☐ Behavioural & social sciences ☒ Ecological, evolutionary & environmental sciences

For a reference copy of the document with all sections, see nature.com/documents/nr-reporting-summary-flat.pdf

Ecological, evolutionary & environmental sciences study design

All studies must disclose on these points even when the disclosure is negative.

Study description	We have designed a photoluminescene-based radiative cooling material that can address the demands of building cooling, aesthetics, urban thermal and visual comfort. The proposed material is a composite with vivid green, yellow, and red colors. It can achieve subambient cooling effect, angle-insensitive appearance, improved urban comfort, and multifunctionalities.
Research sample	N/A
Sampling strategy	N/A
Data collection	For the optical properties, the data was collected by commercial spectrometers with customized modification. For cooling test, the data was collected by commercial data logger. Detailed procedure can be found in Methods and Supplementary Materials.
Timing and spatial scale	For field test, the data was collected in Changchun, China (October 2-4, 2024) and in Hong Kong, China (January 18-20, 2025) during clear sunny days. The temperature was recorded in every 5 minutes. The time and spatial scale are selected to show the universality of the proposed cooling materials.
Data exclusions	No date were excluded.
Reproducibility	For each measurement of the reflectance, the sample was measured for 5 times at the same procedure and be averaged to verify the reproducibility.
Randomization	This is not relevant to our study as all the samples were designed/fabricated/characterized under standard procedures or common routes.
Blinding	This is not relevant to our study because no participant is required for obtaining the results.

Did the study involve field work? ☒ Yes ☐ No

Field work, collection and transport

Field conditions	In both Changchun and Hong Kong, we have selected the rooftop with minimized shading to carry out the filed test. The environmental parameters (ambient temperature, humidity, sunlight) have been given in the paper.
Location	Changchun (43.85 North, 125.41 East) and Hong Kong (22.34 North, 114.17 East)
Access & import/export	N/A
Disturbance	N/A

Reporting for specific materials, systems and methods

We require information from authors about some types of materials, experimental systems and methods used in many studies. Here, indicate whether each material, system or method listed is relevant to your study. If you are not sure if a list item applies to your research, read the appropriate section before selecting a response.

Materials & experimental systems

n/a	Involved in the study
☒	☐ Antibodies
☒	☐ Eukaryotic cell lines
☒	☐ Palaeontology and archaeology
☒	☐ Animals and other organisms
☒	☐ Clinical data
☒	☐ Dual use research of concern
☒	☐ Plants

Methods

n/a	Involved in the study
☒	☐ ChIP-seq
☒	☐ Flow cytometry
☒	☐ MRI-based neuroimaging

Plants

Seed stocks	N/A
Novel plant genotypes	N/A
Authentication	N/A